



OPEN

## Nanotechnology and LSTM machine learning algorithms in advanced fuel spray dynamics in CI engines with different bowl geometries

Harish Venu<sup>1</sup>, Manzoore Elahi M. Soudagar<sup>2,10,12✉</sup>, Tiong Sieh Kiong<sup>1</sup>, N. M. Razali<sup>1,3</sup>, Hua-Rong Wei<sup>13</sup>, Armin Rajabi<sup>1</sup>, V. Dhana Raju<sup>4</sup>, T. M. Yunus Khan<sup>5</sup>, Naif Almakayee<sup>6</sup>, Erdem Cuce<sup>7,8,9,10✉</sup> & Huseyin Seker<sup>11</sup>

This study explores the integration of nanotechnology and Long Short-Term Memory (LSTM) machine learning algorithms to enhance the understanding and optimization of fuel spray dynamics in compression ignition (CI) engines with varying bowl geometries. The incorporation of nanotechnology, through the addition of nanoparticles to conventional fuels, improves fuel atomization, combustion efficiency, and emission control. Simultaneously, LSTM models are employed to analyze and predict the complex spray behavior under diverse operational and geometric conditions. Key parameters, including spray penetration, droplet size distribution, and evaporation rates, are modeled and validated against experimental data. The findings reveal that nanoparticle-enhanced fuels, coupled with LSTM-based predictive analytics, lead to superior combustion performance and lower pollutant formation. This interdisciplinary approach provides a robust framework for designing next-generation CI engines with improved efficiency and sustainability. Diesel engine performance and emissions were found to be influenced by variations in combustion chamber geometry, underwent validation through simulation using Diesel-RK. Re-entrant bowl profile in quaternary blend is found to exhibit 31.3% higher BTE and 8.65% lowered BSFC than the conventional HCC bowl at full load condition. Emission wise, re-entrant bowl induced 90.16% lowered CO, 59.95% lowered HC and 15.48% lowered smoke owing to improved spray penetration and faster burning of soot precursors. However, the NO<sub>x</sub> emissions of DBOPN-TRCC were found to be higher. The simulation outcomes, derived from Diesel-RK, were subsequently compared with empirical data obtained from real-world experiments. These experiments were systematically carried out under identical operating conditions, employing different piston bowl geometries.

**Keywords** LSTM, Diesel-RK, Nano additives, Performance, Emission, Combustion

<sup>1</sup>Institute of Sustainable Energy, Universiti Tenaga Nasional, Jalan IKRAM-UNITEN, 43000 Kajang, Selangor, Malaysia. <sup>2</sup>College of Engineering, Lishui University, 323000 Lishui, Zhejiang, China. <sup>3</sup>AAIBE Chair of Renewable Energy, Universiti Tenaga Nasional, Jalan IKRAM-UNITEN, 43000 Kajang, Selangor, Malaysia. <sup>4</sup>Department of Mechanical Engineering, Lakireddy Bali Reddy College of Engineering, Mylavaram, Andhra Pradesh, India. <sup>5</sup>Department of Mechanical Engineering, College of Engineering, King Khalid University, Abha 61421, Saudi Arabia. <sup>6</sup>Department of Industrial Engineering, King Khalid University, Abha 61421, Saudi Arabia. <sup>7</sup>Department of Mechanical Engineering, Faculty of Engineering and Architecture, Recep Tayyip Erdogan University, Zihni Derin Campus, 53100 Rize, Turkey. <sup>8</sup>Department of Mechanical Engineering, Saveetha School of Engineering, Saveetha Institute of Medical and Technical Sciences, Saveetha University, Chennai 602105, India. <sup>9</sup>University Centre for Research and Development, Chandigarh University, Mohali, Punjab 140413, India. <sup>10</sup>Center for Research Impact & Outcome, Chitkara University, Rajpura, Punjab 140401, India. <sup>11</sup>Department of Information Systems, College of Computing and Informatics, The University of Sharjah, Sharjah, UAE. <sup>12</sup>Division of Research and Development, Lovely Professional University, Phagwara 44411, Punjab, India. <sup>13</sup>Department of Photoelectric Engineering, Lishui University, 323000 Lishui, China. ✉email: manzoor@lsu.edu.cn; erdem.cuce@erdogan.edu.tr

**Abbreviations**

ppm	Parts per million
nm	Nano metre
°CA	Degree crank angle
°C	Celsius (degrees)
nm	Nanometer
ppm	Parts per million
g	Grams
g/kWh	Gram per kilowatt hour
h	Hour
kg	Kilogram
kJ/kg	Kilo Joules per kilogram
kW	Kilowatt
lpm	Liter per minute
mg	Milligram
min	Minutes
m	Meter
mm	Millimeter
MPa	Mega Pascal
N.m	Newton meter
$\eta_{th}$	Thermal efficiency
CO	Carbon monoxide
NO <sub>x</sub>	Oxides of nitrogen
CO <sub>2</sub>	Carbon dioxide
HC	Hydrocarbon
GHG	Green house gases
CEEMDAN	Complete ensemble empirical mode decomposition with adaptive noise
TEM	Transmission electron microscopy
RNN	Recurrent neural network
MAPE	Mean absolute percentage error
CI	Compression ignition
TCC	Toroidal combustion chamber
TiO <sub>2</sub>	Titanium oxide
HRR	Heat release rate
DBOP	Diesel-biodiesel-oil-pentanol blends
DBOPN	DBOP with 20 ppm TiO <sub>2</sub> nano additives
BSFC	Brake specific fuel consumption
BTE	Brake thermal efficiency
CC	Combustion chamber
BTDC	Before top dead centre
DPF	Diesel particulate filter
MAP	Mean average precision
CR	Compression ratio
CP	Cylinder pressure
RSM	Response surface methodology
ANFIS	Adaptive neuro-fuzzy inference system
IP	Injection pressure
IT	Injection timing
SEM	Scanning electron microscopy
R <sup>2</sup>	Coefficient of determination
CRDI	Common rail direct injection
CNT	Carbon nanotube
TRCC	Toroidal re-entrant combustion chamber
HCC	Hemispherical combustion chamber
SDCC	Shallow depth combustion chamber
LSTM	Long short term memory
ANN	Artificial neural network
GA	Genetic algorithm
GRU	Gated recurrent unit network
TDNN	Time delay neural network

Fuel has always been a critical driver of the global economy. Nevertheless, the huge dependence of various industries, particularly the logistics, on fossil fuel and its by-products has brought us to the edge of their depletion. This reliance raises concerns about the negative impacts, including pollution and contributions to global warming through fuel emissions. Consequently, there's an urgent need to establish a robust framework to measure these harmful emissions. Addressing this challenge involves initiatives aimed at developing alternative fuel sources. Recent trends have witnessed a significant upsurge in Bio-fuel research due to its diverse advantages. Beyond reduced emission levels, the ease of manufacturing presents another notable benefit. Various methodologies are being utilized to improve Bio-fuel efficiency and identify the most suitable blends of

fossil fuels. Predictive modeling by AI-ML (Artificial Intelligence-Machine Learning) of engine emissions plays a pivotal role in the quest for the optimal fuel blend. Predictive modeling encompasses generating outcomes through statistical methods and principles of probability. To yield accurate results, this approach necessitates specific input data. The accuracy of a prediction increases with the quantity of test data supplied to the model. The precision of a prediction is a key aspect of determining the model's precision. Additionally, this paper delves into recent technological innovations in the realm of Machine Learning, which synergizes with AI to create a successful precise and concise model.

Ghobadian et al.<sup>1</sup> constructed an ANN trialed model aimed at focusing on the performance and engine emissions as the output with waste vegetable cooking oil based biofuel. The experimental procedure initiated with the production of biofuel after gathering used vegetable cooking oil. This biofuel was introduced to a 2 cylinder diesel engine with emissions and performance parameters were recorded and computed. Diverse blends of biofuels were formulated, with each blend undergoing the same standardized testing protocol. This method generated a substantial volume of data utilized for training the ANN. Following the creation and evaluation of the model, the outcomes demonstrated that the back-propagation algorithm effectively predicted performance parameters. The calculated RMSE root mean error approached 0.0004, closely resembling the ideal value, indicating the accuracy of the predictions made.

Azeez et al.<sup>2</sup> employed an enhanced artificial neural network model for estimating the carbon monoxide (CO) emissions and creating daily restricted maps of a specific area. The exhaust data used in this research originated from the traffic vehicles operating in the designated location. The study introduced hybrid models that integrated data mining and Geospatial Information System (GIS) with a focus on designing, analyzing, and storing various spatial data, etc. In addition, the prediction maps were generated to facilitate the analysis of localized CO emission levels. The model achieved an impressive accuracy rate of 86%, making it a valuable tool for monitoring localized emission predictions from daily traffic vehicles. This model proves highly beneficial in understanding emission patterns, especially when emissions peak, offering valuable insights into harmful emissions' temporal trends. In 2013, a similar approach was adopted<sup>3</sup>, yielding the predictions for a turbocharged engine, encompassing both performance analysis and engine emissions. Similar ANN models were used by various researchers for predicting the performance and emission spectrums<sup>4–6</sup>.

Uslu et al.<sup>7</sup> employed an ANN technique for evaluating the brake power and torque of a SI engine. The research highlighted the scarcity of information concerning the use of iso-amyl alcohol-based fuel. Test rigs were used in experiments to gather exhaust spectrum. Data sets were constructed using altering specific input data, such as throttle, speed, and adjustments in the CR (compression ratio). This dataset was further utilized to train the ANN. For the refinement of the ANN model's performance, they utilized Response Surface Methodology (RSM). The determined correlation factor ranged from 0.94 to 0.99.

Multiple methods, including modeling and simulation, have been employed to estimate diesel engine emissions, broadly sorted for 4 categories: (1) PM and NO<sub>x</sub> sensor calibration<sup>8</sup>; (2) MAP (Mean average precision) -based look-up methods<sup>9</sup>; (3) 0 (or) 3 dimensional modeling<sup>10</sup>; (4) data-driven ML prediction techniques<sup>11</sup>. Radio frequency sensors were also appended by researchers to monitor the DPF (Diesel Particulate Filter), leading to enhanced DPF durability and reduced SFC<sup>12</sup>.

Nevertheless, sensor measurement techniques face challenges such as high expenses and complex structures<sup>13,14</sup>. The commonly used MAP method requires extensive calibration and significant experimental resources, particularly for obtaining precise emission characteristics during transient operations<sup>15</sup>. While modeling methods effectively reduce research time and expenses, they necessitate a deep understanding of complex theories, demanding high expertise from researchers and equipment. Among these methods, data-driven ML approaches have attracted interest owing to benefits: shorter computation time reduced cost, high predictive accuracy, and robustness<sup>16,17</sup>.

This involves using diverse machine learning algorithms to create opaque models for predicting diesel engine emissions without considering operational mechanisms<sup>18</sup>. Machine learning methods provide a balanced trade-off between model accuracy and computational resources during the modeling process, significantly simplifying the complexity of emission prediction<sup>19</sup>. Machine learning techniques have found widespread application across diverse domains, including autonomous driving<sup>19</sup>, electric vehicle charging prediction<sup>20</sup>, language processing<sup>21,22</sup>, face recognition<sup>23</sup>, and traffic flow forecasting<sup>24</sup>. Sangharatna et al.<sup>25</sup> utilized the neural networks (NN) to diagnose faults by detecting and diagnosing engine component status through fault-related signals. Machine learning has been employed to predict diesel emissions since Atkinson<sup>26</sup> developed a NN based prediction model in 1998. Due to the non-linear fitting and generalization capabilities of machine learning methods, they simplify efficient engine optimization<sup>16</sup>, leading to increasing interest from researchers. Table 1 presents an extensive review of literature on the performance and emissions in engine characteristics (not limited to diesel engines) using ML techniques. Early studies mainly relied on data collected from lab engine operations during stable conditions, with the ANN algorithm being predominant<sup>26–28</sup>. Tables 2 and 3 indicate the significance of bowl geometries and nano additives in engine characteristics respectively.

The fuel spray characteristics study is also gaining prominence in recent years as it considers various key factors such that could alter the primary jet formation and atomization process<sup>48</sup>. With higher fuel density, the impinging inertia is improved drastically which could slow down the spray velocity along with higher surface tension which induces cohesive forces and larger Sauter Mean Diameter (SMD) of fuel droplets<sup>49</sup>. Some studies also reveals that, higher fuel viscosity has significant effect on hampering the aerodynamic thrust of the fuel surface and could cause much dawdle in break-up of fuel spray<sup>48</sup>. Highly viscous fuels such as B50 and above could eventually result in higher surface tension and become tough to break up on interaction with air/gas followed by higher STP, lowered SCA and increased SMD<sup>50</sup>. In general, biofuels were blended with volatile fuels to improve the spray properties<sup>51</sup>. Geng et al.<sup>52</sup> found that pure biofuel had a 33.59% higher smoke point (STP) and a 33.08% larger droplet size (SMD) compared to diesel (B0). The addition of 30% ethanol to biodiesel

Researcher	Model used	Fuel used	Input parameters	Output variables/responses	Test dataset and value
Atkinson et al. <sup>26</sup>	ANN	100% diesel	Speed, temperature, rail pressure	Brake power, SFC, emission	MAPE value < 5%
He et al. <sup>28</sup>	ANN	100% diesel	EGR, engine load, injection pressure, engine speed, SOI	Combustion characteristics, NOx emission profile	MSE values: $P_{cyl}$ 0.543, $T_{cyl}$ 28.65, $NO_x$ 58.5
Ivan et al. <sup>29</sup>	RNN	100% diesel	Air-fuel ratio, speed, injection timing advance	Emission: NOx	MAPE value < 2%
Gokhan et al. <sup>30</sup>	GRU	100% diesel	Equivalence ratio, engine speed, SOI, fuel injection rate and quantity, pilot injection	Oxides of nitrogen ( $NO_x$ )	$R^2$ value > 0.75
Yang et al. <sup>31</sup>	LSTM and CEEMDAN	100% diesel	Throttle open rate, SFC, engine speed, torque	Oxides of nitrogen ( $NO_x$ )	MAE value 29.82, RMSE value, 46.11, $R^2$ value 0.98
Tran Van et al. <sup>32</sup>	ANN	Biodiesel blends with diesel and nano additives	Nano additive, engine load, blend composition	Hydrocarbon (HC), carbon monoxide (CO), $NO_{xs}$ emission	$R^2$ value HC 0.86 CO 0.81 $NO_x$ 0.99
Planakis et al. <sup>17</sup>	RNN, TDNN	Pure diesel	Engine speed, air fuel ratio, intake pressure, engine load	Oxides of nitrogen ( $NO_x$ )	$R^2$ value RNN 0.918 TDNN 0.733
Shin et al. <sup>15</sup>	ANN	Pure diesel	Injection pressure, injection timing, IP, intake flow	Emission: $NO_x$	MAPE value: 9.1%
Hao et al. <sup>33</sup>	LSTM	Pure diesel	Air fuel ratio, relative speed, engine torque, oil/coolant, exhaust temperature	Emission: HC, CO and NO	$R^2$ value HC 0.93 CO 0.81 NO 0.85
Joseba et al. <sup>34</sup>	ANN	Pure diesel	Engine speed, torque, rail pressure, ambient pressure, relative humidity	Performance: BSFC Emission: CO, $CO_2$ , $NO_x$	$R^2$ value BSFC 0.98 CO 0.76 $CO_2$ 0.89 $NO_x$ 0.85

**Table 1.** Overview of model used along with test dataset values.

Researcher	Geometry used	Fuel/experiment or simulation	Parameters employed	Significance
Saito et al. <sup>35</sup>	Re-entrant chamber	100% diesel (experimental)	Shall depth and re-entrance CC	Lowered BSFC, less emissions
Zhu et al. <sup>36</sup>	TRCC	100% diesel (experimental)	Pip area, torus radius, piston bowl lip area	Improved air-fuel mixing, lowered emission, high performance
Dolak et al. <sup>37</sup>	Stepped bowl chamber	100% diesel (simulation)	Swirl, modified spray angle, fuel injection rate	Lowered SFC at part and full load, less CO and soot precursors
Lim et al. <sup>38</sup>	Bowl-in-piston (Mexican hat shaped)	100% diesel (simulation)	Different spray angles (70, 100 and 130 deg)	Lowered NOx emissions and soot (about 6.8%) for 70 deg spray angle with Mexican hat shaped geometry
Shi et al. <sup>39</sup>	Quiescent	100% diesel (experimental)	Swirl ratio induction, spray target with part and high load variation	Full load with swirl resulted in higher performance and minimized emissions
Wickman et al. <sup>40</sup>	Re-entrant chamber	100% diesel (simulation)	EGR, Swirl ratio, SOI, injection pressure and compression ratio	Lowered BSFC, CO, $NO_x$ and $CO_2$

**Table 2.** Overview of various bowl geometries and their significances<sup>35–40</sup>

resulted in a substantial decrease in its kinematic viscosity and surface tension, leading to a notable improvement in the spray breakup. Hence, the B70E30 exhibited a decrease of 22.05% in its STP and a decrease of 20.88% in its SMD, when compared to B100. Multiple studies have shown that biodiesel has ↑STP, ↓SCA, ↑SMD, and less velocity of fuel injection with respect to mineral diesel<sup>[53,54]</sup>. For instance, Raghu et al.<sup>55</sup> examined spray properties of biofuels and verified that biofuels have ↑STP and ↓SCA compared to diesel<sup>55</sup>.

### Novelty of the current research

In spite of several investigations delved into alternative fuel with machine learning, this particular study aims to explore quaternary fuel as the primary fuel doped with nano particle with various bowl geometries. With limited prior research delving into the combination of biofuel and nano additives, key focus of present work is to analyze the impact of introducing the nano biofuel in various bowl geometries on diesel engine behavior and performance. Apart from standard hemispherical bowl, toroidal, shallow depth and toroidal re-entrant profiles were evaluated. The gathered data underwent analysis using a machine learning approach that utilized the Long Short-Term Memory (LSTM) model within an artificial neural network framework across various engine loading conditions. Also, using Diesel-RK combustion simulation software, the fuel spray characteristics were studied for various bowl profiles and the results were compared.

Researcher	Nano additive and surfactant concentration	Base fuel and surfactant	Engine specification	Significance
Sivakumar et al. <sup>41</sup>	Al <sub>2</sub> O <sub>3</sub> (50–100 ppm), Cetyltrimethyl ammonium bromide	Palm oil methyl ester	Single cylinder, 4 S, Kirloskar AV1, 210 bar IP and 23degTDC IT, 16.5:1 CR, 1500 rpm	7% high BTE, lowered BSFC, HC, CO, higher NO <sub>x</sub> emissions
Ranjan et al. <sup>42</sup>	MgO (30 ppm), 4-chlorobenzoyl chloride	Waste cooking oil biodiesel	Single cylinder, Kirloskar TV1, vertical, 1500 rpm, 17:1 CR, load (4.7–18.11 kg)	Higher BP, BSFC and BTE, CO <sub>2</sub> , lowered HC, CO and NO <sub>x</sub> , improved combustion
Mehreganet al. <sup>43</sup>	Manganese oxide and cobalt oxide (25 ppm and 50 ppm), no surfactant	B20 Waste frying oil	4 cylinder, 4 stroke urea-SCR direct injection, CR 17.9: 1, IP210 bar, IT 23 deg bTDC	Lowered SFC at part and full load, higher thermal η, drastic reduction of NO <sub>x</sub> and CO.
El-Seesy et al. <sup>44</sup>	Al <sub>2</sub> O <sub>3</sub> (50–100 ppm), 20 mg per litre, no surfactant	Jojoba oil methyl ester	Deutz F11511, 1 cyl, 4 S, DI, 1500 rpm, IP175 bar, IT 24 deg bTDC	NO <sub>x</sub> 70%↓, CO 80%↓, HC 60%↓, and Smoke 35%↓, 12% drop in BSFC
Hoseini et al. <sup>45</sup>	Graphene oxide (30, 60 and 90 ppm), no surfactant	Ailanthus altissima biodiesel	Lombardini Diesel 3LD510, 1800 rpm, 17.9:1 CR, 1 cyl, non-turbocharged, 32.8 Nm torque	↓HC, ↓CO, ↓BSFC, ↑NO <sub>x</sub> and ↑CO
Kumar et al. <sup>46</sup>	Ferrous oxide and ferrofluid (0.5%, 1% and 1.5%), Surfactant: 2 mol of NaOH	B20 palm oil methyl ester	Single cylinder, 4 S, Kirloskar TV1, 210 bar IP and 23degTDC IT, 16.5:1 CR, 1500 rpm	↑ BTE (by 16.6%), ↓BSFC (by 11.1%), other emissions reduced simultaneously
Ashok et al. <sup>47</sup>	Zinc oxide (50 and 100 ppm), Ethanox (200 and 500 ppm) Surfactant: Alcohol	CalophyllumInophyllum methyl ester	Simpson S217, Two cyl 4 S, DI, vertical, IT 23 deg bTDC, IP 200 bar 18.5:1 CR	High BTE for ZnO (29.5%) than Ethanox (26.8%), lowest BSFC for ZnO 50 ppm, 18.4% and 13% less CO and HC for ZnO 50 ppm, 17.8% less NO <sub>x</sub> for Ethanox (500 ppm), 12.6% less NO <sub>x</sub> for ZnO100ppm.

**Table 3.** Overview of a variety of nano additives and their influence on characteristics of engine<sup>41–47</sup>

Properties	ASTM method	Diesel	jatropha oil	Jatropha biodiesel	Pentanol
Density at 20 °C, kg/m <sup>3</sup>	D1298	840	940	874	814
Kinematic viscosity at 40 °C, cSt	D445	2.84	24.5	4.34	2.88
Heating value, kJ/kg	D240	44,705	38,650	42,673	35,164
Flash point, °C	D93	68	225	130	33
Cetane number	D613	48	38	53	20
Iodine value, gI <sub>2</sub> /100 g	D1959	0.15	97.2	0.26	—
Carbon residue (%)	D524	0.12	1.0	0.25	—
C/H ratio (by vol)	D5291	6.52	6.54	6.93	4.96
Acid value, mg KOH/g	D974	—	3.83	0.40	—
Elemental analysis (%wt)					
C (%)		80.12	76.99	82.22	68.12
H (%)		12.2	11.77	11.96	13.72
O (%)		1.21	10.58	5.74	18.15
N (%)		1.68	0.66	0.041	—
S (%)		4.79	—	0.038	—

**Table 4.** Physical properties of diesel, Jatropha vegetable oil and Jatropha biodiesel (Data sourced from<sup>56</sup>).

## Materials and methods

### Test fuel preparation

The test fuel employed for the current experimentation is a quaternary blend of diesel/biodiesel/vegetable oil/pentanol and termed as DBOP blend. The DBOP blend is comprised of 50% diesel (vol%) + 5% biodiesel (vol%) + 5% vegetable oil (vol%) + 40% (vol%) pentanol. This combination is selected based on fuel properties and experimentation from previously published data<sup>56</sup>. DBOPN is prepared by blending 20ppm TiO<sub>2</sub> nano additives with DBOP blend. TiO<sub>2</sub> nano additives were chosen as specific additive due to its improved oxidation at higher cylinder temperatures so that it can act as a buffer O<sub>2</sub> for promoting oxidation. Also, the 20ppm concentration is opted based on experimentation and fuel property analysis. The blends were initially prepared using magnetic stirrer followed by ultrasonication. The blends were then checked for stability. The blends were initially found to be stable for 48 h. Then, surfactant Span80 + Tween 20 was added to the blend at concentration of 5 mg/L. After this, the blends were found to be stable for more than 120 h. The fuel properties of the test fuel blend, physio-chemical properties and properties of test fuel blends were displayed in Tables 4, 5 and 6. The above blend has been chosen owing to the fact that it has highest Brake thermal efficiency than other blend concentrations, lowered BSFC, HC, CO and Smoke opacity (indicated by Ref<sup>56</sup>). However, the NO<sub>x</sub> profile of DBOP40 is higher for which the current work employs the usage of various bowl geometries and nano additives and their influence is studied and validated by LSTM (Long Short Term Memory) machine learning algorithm.

### Nanoparticle preparation and characterization

First, the precursor ingredient, titanium tetraisopropoxide, is neutralised with ethanol, hydrochloric acid, and deionised water. This was followed by thirty minutes of vigorous stirring to lower the pH of the liquid to 1.5.

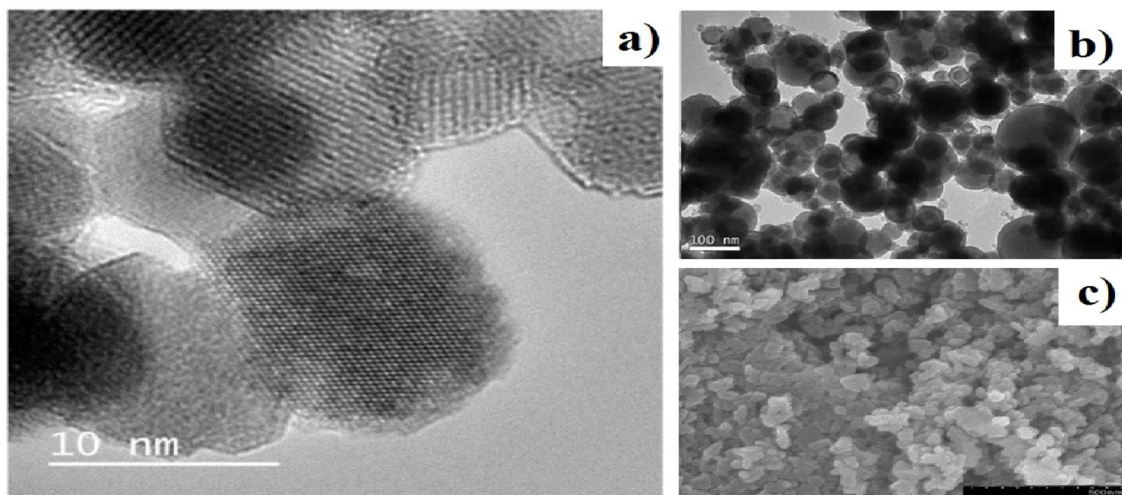
Fuel properties	ASTM method	D50B50	DBOP10	DBOP20	DBOP30	DBOP40 (represented as DBOP)
Density (kg/m <sup>3</sup> )	D1298	859	851	846	841	834
Kinematic viscosity (cSt)	D445	3.27	3.38	3.49	3.60	3.71
Calorific value (kJ/kg)	D240	43,146	43,526	43,716	44,076	44,456
Cetane number	D613	50.25	49.3	48.35	47.4	46.45
Flash point (°C)	D93	98.7	92.5	86.3	80.1	73.9

**Table 5.** Physio-chemical properties of test fuels (Data sourced from<sup>56</sup>).

Fuel properties	ASTM method	DBOP40	DBOP40+10 ppm TiO <sub>2</sub>	DBOP40 + 20 ppm TiO <sub>2</sub> (represented as DBOPN)	DBOP40+30 ppm TiO <sub>2</sub>
Density (kg/m <sup>3</sup> )	D1298	834	831	830	827
Kinematic viscosity (cSt)	D445	3.71	3.58	3.52	3.23
Calorific value (kJ/kg)	D240	44,456	44,652	45,017	44,841
Cetane number	D613	46.45	46.7	46.8	46.5
Flash point (°C)	D93	73.9	75	78	77

**Table 6.** Properties of fuel blends with nano particle.

Property	ASTM method	Value
Colour	–	White
Particle size, average (nm)	E3247	19–24
Purity (%)	D476	96.99
Specific surface area (m <sup>2</sup> /g)	C1069	372
Bulk/true density (g/cc)	D7263	0.18
Microstrain ( $\xi$ )	D4892	0.084
Dislocation density ( $\delta$ ) (line <sup>2</sup> /m <sup>2</sup> )	E2208	$0.5 \times 10^{14}$

**Table 7.** TiO<sub>2</sub> nano particle properties (Data sourced from<sup>57</sup>).**Fig. 1.** (a) HR-TEM, (b) TEM, (c) SEM of TiO<sub>2</sub>nano particles<sup>57</sup>

The pH level was then raised to six after two hours of continuous stirring and the addition of 10 mL of deionised water at room temperature. Once another titration with demineralized water was completed, cladigel was produced; its pH was 8. Next, for a whole day at 150 °C, the cladigel was dried and calcined. TiO<sub>2</sub> nanoparticles were finally produced by heating the dried samples to 300 °C for two hours. The manufactured TiO<sub>2</sub> nanoparticles' physical properties are described in more detail in Table 7.

Distinct lattice fringes were revealed by HR-TEM and TEM morphology (Fig. 1a, b) using the JEM-3010 ultra-high-resolution analytical electron microscope, showing the presence of nano crystalline TiO<sub>2</sub> particles.

An inconsistent spherical distribution of nano particles with mild aggregation was apparent in the SEM picture (Fig. 1c) produced using the VEGA3-TESCAN preparation. Figure 2 depicts the outcomes of the energy dispersive spectrum analysis (EDX) of  $\text{TiO}_2$  nano particles (Make: INCA Energy 250 micro analysis equipment), which verifies that the composition contains just titanium and oxygen components and does not contain any observable contamination.

### Experimental setup

An agricultural based single-cylinder, four-stroke compression–ignition engine is used in this investigation. The engine configuration is depicted in Fig. 3, and the test engine's parameters are listed in Table 8. Emission, performance, and combustion characteristics of the engine when running on a blend of DBOP enhanced with  $\text{TiO}_2$  nano additions are the primary objectives. A dynamometer is connected to the engine, and the position of the crank angle is continuously monitored by a crank angle encoder. Water cooling systems are installed in both the engine and the dynamometer. On the vertical surface of the cylinder, an in-cylinder pressure transducer is mounted in order to measure the maximum pressure. Furthermore, a system that incorporates an electronic control unit to regulate crucial engine operating parameters, such as the IT (injection timing) and IP (injection pressure). A high-speed Data Acquisition System (DAS) is utilized for the collection and recording of combustion-related data, encompassing cylinder pressure fluctuations, Heat Release Rate (HRR), and Cumulative Heat Release Rate (CHRR). The quantification of regulated emissions such as HC, CO,  $\text{CO}_2$ ,  $\text{NO}_x$ , and smoke is conducted through AVL gas analyzers and a Bosch smoke meter.

### Combustion bowl alteration

The main reason for combustion chamber geometry in the cylinder piston is to enhance the turbulence results in better mixing of air/fuel. During the first two strokes, suction of air takes place at a very high-pressure and has several motion turbulences which eventually results in a heated air. These typical erratic motions were widely dependent on bowl geometries as the movement of air is pretty random in topmost area of piston. At the end of the second stroke, only the fuel is supplied where these turbulent air mixtures uphold evaporation and vaporization phenomenon. For the present experimentation, different bowls were considered namely TCC, TRCC and SDRCC with a constant volume of 661 cc equivalent to that of standard HCC. Hence, compression ratio is also held constant. The different combustion chamber geometries were illustrated in Fig. 4.

### LSTM network—an overview

Time series data is a frequently encountered data format. Among the various sectors and applications that LSTM covers are finance, health monitoring, demand and supply forecasting, and other disciplines. In the context

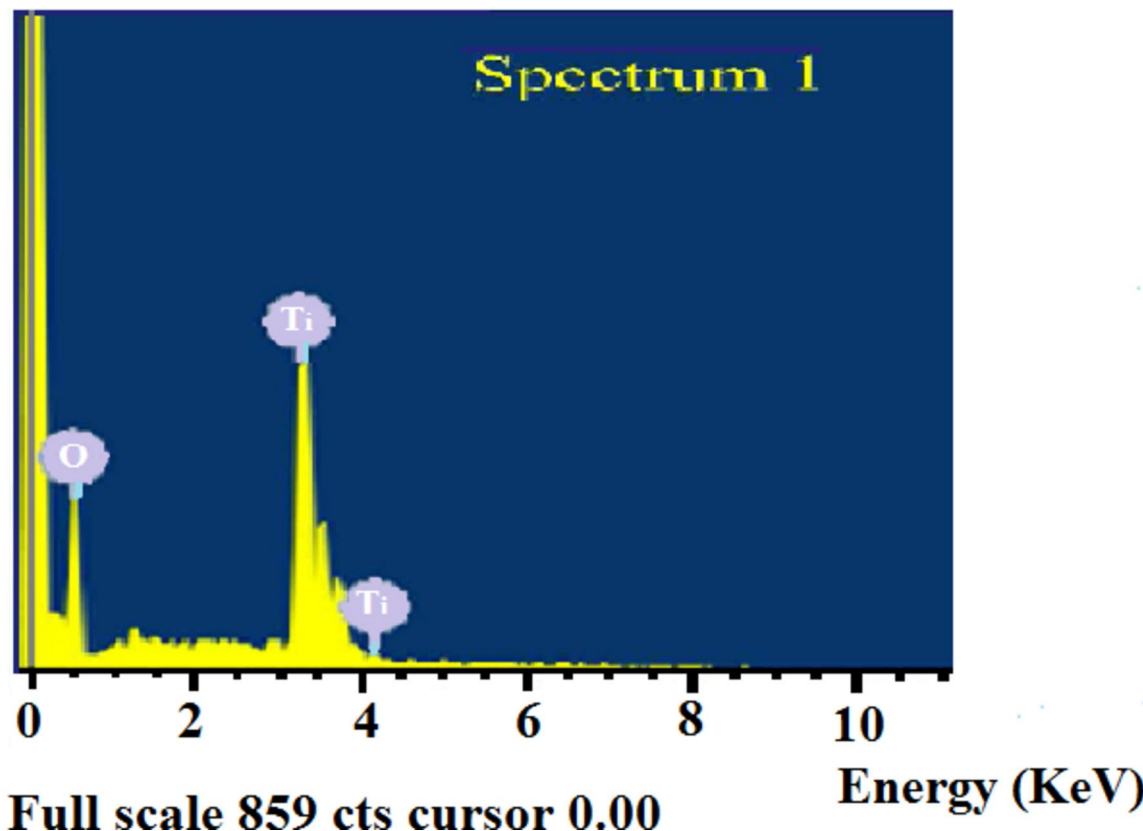
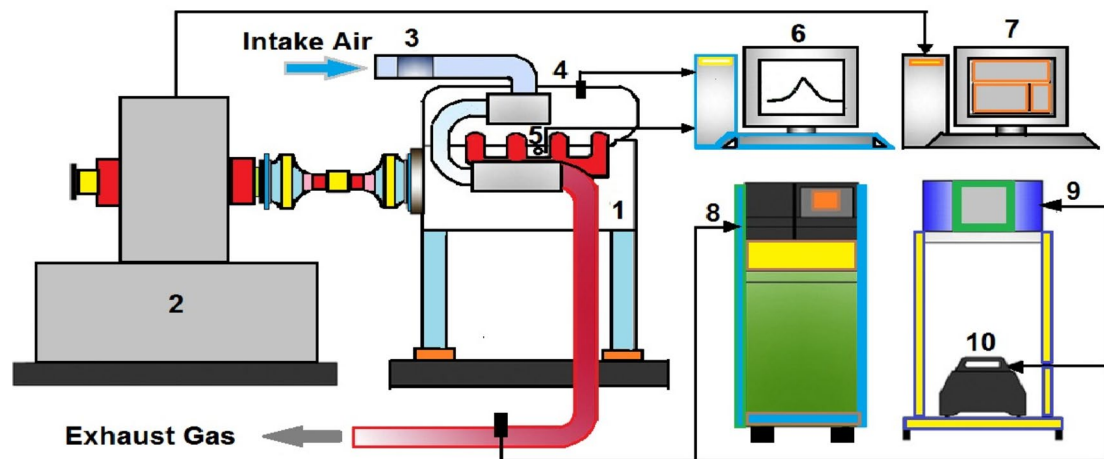


**Fig. 2.** Energy dispersive spectrum analysis (EDX) of  $\text{TiO}_2$  nano particles<sup>57</sup>



- |                                    |  |
|------------------------------------|--|
| <b>1. Test engine</b>              | <b>6. Data aquisition system (DAS)</b> |
| <b>2. Eddy current dynamometer</b> | <b>7. Dynamometer controller</b>       |
| <b>3. Air mass sensor</b>          | <b>8. Bosch gas analyser</b>           |
| <b>4. Pressure sensor</b>          | <b>9. AVL digas analyser</b>           |
| <b>5. Accelerometer</b>            | <b>10. Smoke opacity meter</b>         |

**Fig. 3.** Schematic of the experimental setup.

Type	Kirloskar, four stroke DI diesel engine
Bore × stroke	87.5 mm × 110 mm
Number of nozzle holes	3
Stroke volume	661 cc
Geometry of piston	Hemispherical
Injection timing	23° bTDC
Injection pressure	200 bar
Cone angle of fuel spray	120°
Compression ratio	17.5:1
Nozzle spray hole diameter	0.3 mm
Inlet valve open	4.5° before TDC
Inlet valve close	35.5° after BDC
Rated power	4.4 kW
Rated speed	1500 rpm
Exhaust valve open	35.5° before BDC
Exhaust valve close	4.5° after TDC

**Table 8.** Test engine specification.

of time series analysis, a common task involves forecasting future values by utilizing historical data, typically when presented with a historical array of time series values. Time series forecasting techniques branches into two primary domains: those that rely on machine learning models and those that adhere to traditional statistic methods. While the latter recurrent neural networks (RNNs), is commonly utilized to detect, classify, and forecast anomalies in time series data.

RNNs are purposefully crafted to improve the processing of sequential data by considering the intrinsic sequential structure of the dataset. Within a conventional RNN network, the calculation proceeds sequentially from the initial sequence element to the last one, advancing one step at a time. At each step, it takes in two inputs: In the context of a basic LSTM, the input consists of current succession element and the output generated by the preceding sequence element. These inputs may be represented as numerical values or textual descriptions. The LSTM layer is usually sandwiched amid input &output layers. A deep LSTM network's LSTM layer configuration can be altered to meet the requirements of a given application. Deep LSTM performs well over the basic LSTM

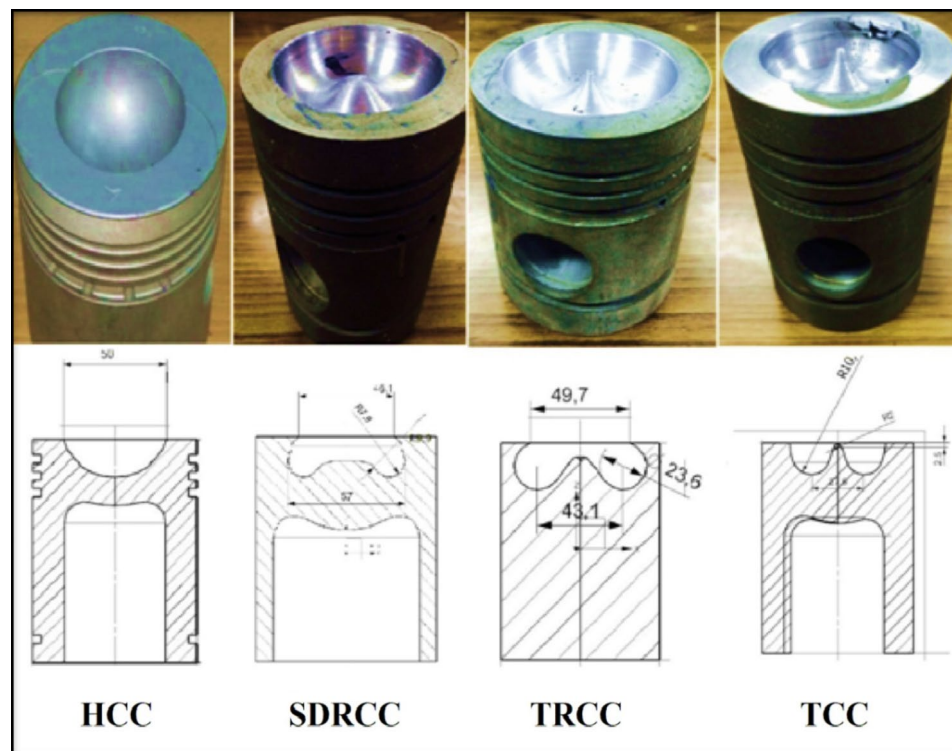


**Fig. 4.** Pictorial representations of modified piston bowl geometries<sup>58</sup>

due to the fact that it can process input values through time in a single LSTM cell as well as across numerous LSTM layers.

Thus, each time step's inputs undergo a thorough processing due to the layers' equitable distribution of the input variables. Recurrent Forecast Layer (RFL) is a subset of LSTM. To address the computational complexity issues associated with employing a conventional LSTM RNN at each time step, this novel architectural design was created. The final design (Deep LSTM with a Recurrent Projection Layer) has some LSTM layers with separate projection layers for each LSTM layer. Due to its ability to progress the model's efficiency with greater depth, this arrangement is quite advantageous when handling excess storage demands. Increased depth also acts as a safeguard against over-fitting in models since it necessitates inputs to pass through a variety of non-linear functions in these networks.

LSTM models require intensive training by related datasets before they are suitable for use in real-world applications. Word sequences can be processed for purposes such as language modeling and text production. Linguistic models can operate effectively about multiple levels and even entire page. Also, noteworthy use pertains to processing of characters/images, where an input image undergoes analysis to create captions and sentences customized to that image. This entails the utilization of a dataset containing a multitude of images for training a specially crafted LSTM model, in conjunction with its associated descriptive captions. Following this, when new sets of images are presented to the model, it generates captions for these images. The model's accuracy is contingent upon a range of parameters, encompassing the quantity of secreted layers, duration of training epoch and solver optimization.

LSTMs find another application akin to their role in text generation, and this pertains to the domain of music generation. In this scenario, LSTM networks predict musical notes by scrutinizing combinations of input notes. When it comes to language translation, LSTM's facilitate the mapping of the sequence order of phrases from one language to its corresponding order in another language. Model training involves using a refined subset of the dataset that includes phrases and their translations after data cleaning. Before being produced as a transformed version, the input data undergoes conversion into a vector representation through an LSTM model. Generally, RNNs employ multiple layers, each encompassing functions like sigmoid, multiplication, and addition.

Within this architecture, data moves sequentially, transitioning from  $C_{t-1}$  till  $C_t$ , and this process involves the utilization of various parameters such as tan h, the sigma function, the value 1 (which allows data to pass through a sigmoid layer), and the value 0 (which prevents data transfer between consecutive stages). LSTM, as a subtype of recurrent neural networks, relies on long-term memory and has garnered substantial popularity across diverse fields when related with alternative models. In an ideal scenario, RNN incorporates multiple layers, each containing a 1 layer sigmoid function, multiplication, and subtraction. The math-model is displayed following the guidelines outlined in Ref<sup>59</sup>.

The LSTM architecture is shown clearly in Fig. 4. Within an LSTM, there are three gates which are controlled by the sigmoid activation function, functioning within a range from 0 to 1. In this range, a value of 0 acts as

a barrier preventing incoming data, while a value of 1 allows data to pass freely. This function is purposefully crafted to generate a positive output, ensuring accurate and precise outcomes.

$$i_t = s(w_i[A_{t-1}, S_t] + b_i) \quad (1)$$

$$f_t = s(w_f[A_{t-1}, S_t] + b_f) \quad (2)$$

$$o_t = s(w_o[A_{t-1}, S_t] + b_o) \quad (3)$$

In the provided equations, the left-hand side (LHS) represents the input, forget, and output gates, denoted by the variables ‘i’, ‘f’, and ‘o’. The symbol sigma ( $\sigma$ ) is used to signify the sigmoid activation function. The symbol ‘w’ stands for the weights assigned to the neurons within these respective gates. ‘At-1’ corresponds to the hidden state of the previous unit at time, ‘t-1’, while ‘St’ represents the input at the current time step. The symbol ‘b’ represents the biases linked to the three gates, as indicated in Fig. 5 with values 0, 1, 2, and 3.

Additionally, Eq. (1) delineates how the input gate determines the nature of the information to be carried forward. Equation (2) quantifies the degree to which the current unit should forget past information from the previous unit. Lastly, Eq. (3) governs the activation of the output gate for the current time step.

$$\tilde{C}_t = \tan h(w_c [A_{t-1}, S_t] + b_c) \quad (4)$$

$$C_t = f_t * C_{t-1} + i_t * \tilde{C}_t \quad (5)$$

$$A_t = o_t * \tan h(C_t) \quad (6)$$

The variable  $C_t$  stands for the memory information at the present time step, and  $\tilde{C}_t$  represents the candidate for the current cell state. The symbol ‘\*’ indicates element-wise multiplication of the given vectors.

Upon scrutiny of Eqs. (4)–(6), it becomes apparent that the activation function in Eq. (8) assumes a vital role in deciding what information to discard and in shaping the final output, based on the previous memory state.

LSTM comparing to other models, has layer memory, and each output rely upon prior outputs which has potential to exploit the dependencies between time series data. In engine emission prediction, LSTM will be an add-on benefit as it has gated mechanism, long term-dependency handling, versatility and lesser gradient problems.

### Diesel RK—software: fuel spray visualization

Diesel-RK simulation software is a top-notch tool for optimizing parameters linked to Compression Ignition (CI) engines because it is primarily made to imitate the real-world operational scenarios of diesel engines. Estimating diesel engine performance, combustion dynamics, and emission characteristics is the primary use. It operates on both conventional diesel fuel and a wide range of biodiesel categories. In particular, Diesel-RK is able to replicate the running cycles of a number of diesel engines without much dependence on empirical coefficients. These coefficients hold constant for a wide range of engine types and operating situations. Modern models for combustion and emission production are included in the strategy, along with strategies for optimization that insure adherence to existing emission regulations. It permits optimal emission control and conforms with current regulations.

Diesel-RK is unique in that it can imitate several combustion chamber geometries, encompassing nozzle, spray placement, swirl profiles, and multiple fuel injections. It is also a beneficial tool for maximizing piston

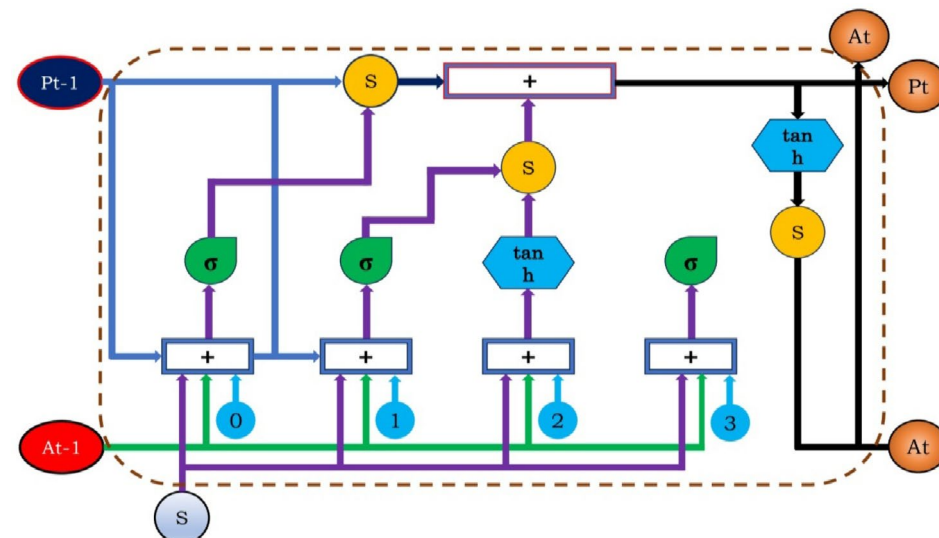


**Fig. 5.** LSTM architecture.

bowl shapes that comply with certain design specifications. Also, the software provides dynamic visualizations that demonstrate connections between adjacent sprays, air swirl patterns, and chamber walls and fuel sprays. A range of fuel substitutes enable an in-depth evaluation of diesel engine properties, such as thermal efficiency, in-cylinder pressure, heat release rates, ignition delays, and concentrations of soot, CO, and NO<sub>x</sub>. Therefore, by correlating these simulation results with experimental test data, exact inferences can be made. Without modifying the engine's running conditions, Diesel-RK makes it less difficult to generate piston bowls with Hemispherical Combustion Chambers (HCC) that meet testing requirements during the experimental phase.

By using default data on widely accepted technical solutions for internal combustion engines and general diesel engine knowledge, Diesel-RK streamlines the development of input data files. This simplifies the process of entering data and calibrating the engine model. It is regarded as a professional tool of the industry, which makes it indispensable for researchers working on projects with tight deadlines and sparse experimental data. It uses combustion modeling and spray evolution simulations to take use of the physical characteristics of biofuel blends. Additionally, users can designate distinct fuels for different engine running modes and preserve bespoke fuel attributes in the internal database of the software. It introduces an alternative concept known as the multi-Zone quasi-dimensional model (as shown in Fig. 6), which partitions sprays into distinct zones based on a combination of geometric principles and considerations related to mixture formation and evaporation conditions. The figure provides a comprehensive overview of the multi-zone fuel spray model, which reveals the existence of seven distinct characteristic zones that correspond to specific evaporation and combustion conditions. Before the fuel jet makes contact with the surface (jet impingement), there are only three zones in the spray:

1. The free spray's thick axial core.
2. The free spray's thick forward front.
3. An outer sleeve that is diluted and encircles the free spray.

However, once the jet impinges on a nearby surface, the flow becomes more homogeneous and denser, leading to a further classification into four zones:

4. An axial conical core of the near-wall flow.
5. The flow's thick core approaches the wall.
6. The near-wall flow's dense forward front.
7. A diluted outer zone encircling the flow close to the wall.

Throughout its development, the spray eventually reaches both the cylinder liner and the cylinder head, completing its trajectory. Figure 7 illustrates the design of piston bowl for (a) HCC (b) SDCC, (c) TCC and d) TRCC with Diesel-RK software.

The capacity of the engine simulation program DIESEL-RK to forecast the performance, combustion dynamics, and emission features of diesel engines running on different fuels under optimal conditions has recently brought it notoriety. Using the extensive thermodynamic engine simulation program DIESEL-RK, Al-Dawody and Bhatti<sup>60</sup> investigated creative methods for cutting NO<sub>x</sub> emissions. They recommended designing deeper piston bowls with smaller diameters based on their simulation tests, which showed a considerable reduction in nitrogen oxide emissions.

In an alternative investigation, Kuleshov<sup>61</sup> conducted a thorough examination of diesel engine performance and emission characteristics under typical operating settings using DIESEL-RK simulation software. They found that the software may be a very useful tool for changing a lot of engine characteristics, such as fuel injection, nozzle count, exhaust gas recirculation, and piston bowl shape. Additionally, Venu et al.'s study<sup>62</sup> looked at how emissions, combustion, and diesel engine performance are affected by the architecture of the combustion chamber. They performed engine experiments and simulations under similar operating conditions using the simulation system. With regard to the combustion chamber design, their work expands the body of knowledge regarding the software's ability to analyze performance and optimize emissions of diesel engines.

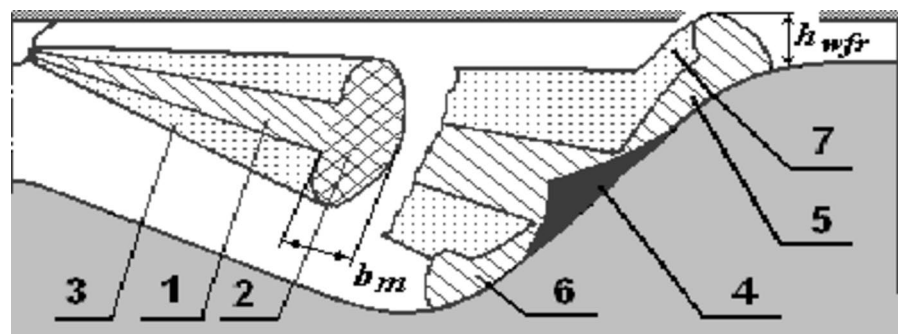


**Fig. 6.** Multi zone-fuel spray model developed by Diesel-RK simulation<sup>58</sup>

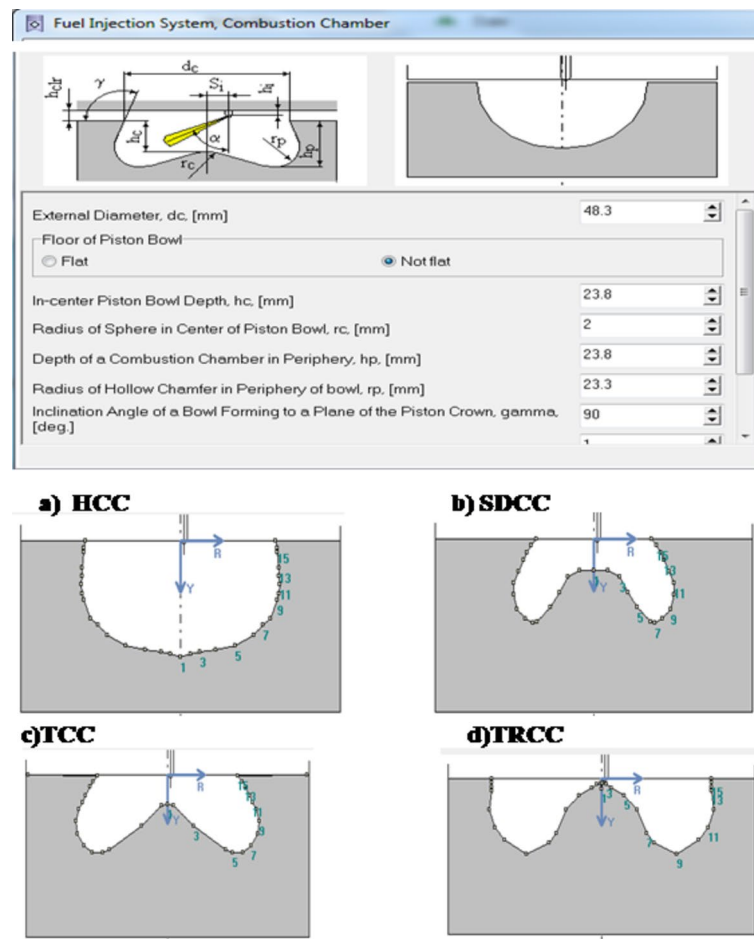


**Fig. 7.** Different combustion chamber geometries design using DIESEL-RK software.

### Uncertainty analysis

Errors and uncertainties can emerge from various factors like selection and calibration of instruments, changing environment conditions, tests and observations, etc. In general, uncertainty can be grouped into two major factors, namely fixed errors and random errors. The former scenario deals with repeatability while the latter deals with the analytical measurements. In this current work, the uncertainty of measured variable ( $\rho X$ ) is evaluated by Gaussian distribution as shown in Eq. (7) within the confidence limits of  $\pm 2\sigma$ .  $2\sigma$  is the mean limit in which the 95% of measured values rely upon.

$$\Delta X_i = \frac{2\sigma_i}{X_i} \times 100, \quad (7)$$

where  $X_i$  is the number of readings,  $\bar{X}_i$  denotes the experimental reading and  $\sigma_i$  represents standard deviation. The uncertainties of calculated parameters were assessed using the expression given below:

$$R = f(X_1, X_2, X_3, \dots, X_n) \quad (8)$$

$$\Delta R = \sqrt{\left[ \left( \frac{\partial R}{\partial X_1} \Delta X_1 \right)^2 + \left( \frac{\partial R}{\partial X_2} \Delta X_2 \right)^2 + \left( \frac{\partial R}{\partial X_3} \Delta X_3 \right)^2 + \dots + \left( \frac{\partial R}{\partial X_n} \Delta X_n \right)^2 \right]}, \quad (9)$$

where  $R$  in Eq. (8) represents the function of  $X_1, X_2, \dots, X_n$  and  $X_1, X_2, \dots, X_n$  represents number of readings taken. Hence “ $\rho R$ ” is computed by RMS (root mean square) of errors associated with measured parameters. The uncertainties of various measuring instruments were illustrated in Table 9. By using Eq. (9), the uncertainties in various measured parameters were evaluated and tabulated in Table 10.

Instruments	Ranges	Accuracy	% Uncertainty
Stopwatch	–	+0.5s	0.2
Manometer	0–200 mm	+1 mm	1
Tachometer	0–10,000 rev/min	+10 rpm	0.1
Smoke meter	0–100 BSU	+0.1	1
Exhaust gas temperature	0–900 °C	+1 °C	0.12
Pressure transducer	0–110 bar	+0.1 bar	0.2

**Table 9.** Uncertainty values of instruments.

Parameters	% Uncertainty
Speed	0.2
Load	0.52
Brake power	0.36
Brake specific fuel consumption	0.4
Brake thermal efficiency	0.34
Fuel flow rate	0.68
Air flow rate	0.58
Carbon monoxide	0.2
Oxides of nitrogen	0.3
Hydrocarbon	0.5
Smoke opacity	0.9

**Table 10.** Uncertainty values of parameters.

## Results and discussion

### Performance characteristics

#### *BSFC (brake specific fuel consumption)*

The variation of BSFC for DBOPN in different combustion chamber geometries for the examined fuel samples were shown in Fig. 8. It is inferred that with increment in load, the BSFC was decreased owing to elevated cylinder temperature at peak loads thus requiring less fuel to maintain a constant speed. Among different geometries, it is found that, apart from HCC, the TCC geometry exhibits higher fuel consumption due to lacking pace in induction of swirl. At full engine load condition, the BSFC of DBOPN-TCC, DBOPN-SDCC and DBOPN-TRCC were lower than DBOPN-HCC by about 3.74%, 5.63% and 8.65% respectively. The toroidal re-entrant bowl profile boosted the engine performance due to improvements in air-fuel mixture formation and more of this mixture is being directed concerning with ignition zone and better mixing of fuel/air mixture. Overall, contemplating BTE and BSFC variation, DBOPN-TRCC is considered the best blend for improved performance.

These are on par with the findings of Jaichandar and Annamalai<sup>63</sup> and Wickman et al.<sup>40</sup>. With toroidal re-entrant bowl geometry, the BSFC is found to increase in the literature of Lalvani et al.<sup>64</sup>. However, some contradictory results with toroidal re-entrant bowl geometry giving rise to lowered BSFC such as Mamilla et al.<sup>65</sup>, Bapu et al.<sup>66</sup> and Venkateswaran and Nagarajan<sup>67</sup> which is a result of abnormal fluctuation in swirl and turbulence resulting in reduced combustion efficiency and more fuel enters the combustion chamber to maintain engine speed constant giving rise to lowered BSFC profile.

#### *BTE (brake thermal efficiency)*

Figure 9 illustrates the variation in Brake Thermal Efficiency (BTE) for DBOPN across various combustion chamber geometries in relation to engine load. The results highlight the crucial role of the combustion chamber in enhancing engine efficiency. In comparison to DBOPN-HCC, DBOPN-TRCC, DBOPN-SDCC, and DBOPN-TCC demonstrated higher BTE values by approximately 8.4%, 5.89% and 3.11% respectively, at full engine load conditions. This improvement is attributed to enhanced swirl and squish motion, facilitating improved air-fuel mixing with the modified chamber geometry. Notably, the TRCC bowl stands out as consistently yielding higher BTE across the entire engine load range among the various combustion chamber configurations; Brake thermal efficiency of DBOPN-TRCC is more than DBOPN-HCC and DBOP by about 8.4% and 11.97% respectively. This is because the re-entrant profile of TRCC offers fuel turbulence with an enhanced swirl. DBOPN-TRCC exhibits 33.484% BTE at 100% engine load condition with impact of fuel bound oxygen atoms in BFB improving efficiency of combustion along with higher BTE. These results are on par with the findings of Jaichandar and Annamalai<sup>63</sup> and Venkateswaran and Nagarajan<sup>67</sup>. With toroidal re-entrant bowl geometry, the BTE is found to increase in the literatures of Mamilla et al.<sup>65</sup>, Bapu et al.<sup>66</sup> and Venkateswaran and Nagarajan<sup>67</sup>. However, some contradictory results with toroidal re-entrant bowl geometry giving rise to lowered BTE were reported such as Lalvani et al.<sup>64</sup>. However, some contradictory results with toroidal re-entrant bowl geometry giving rise

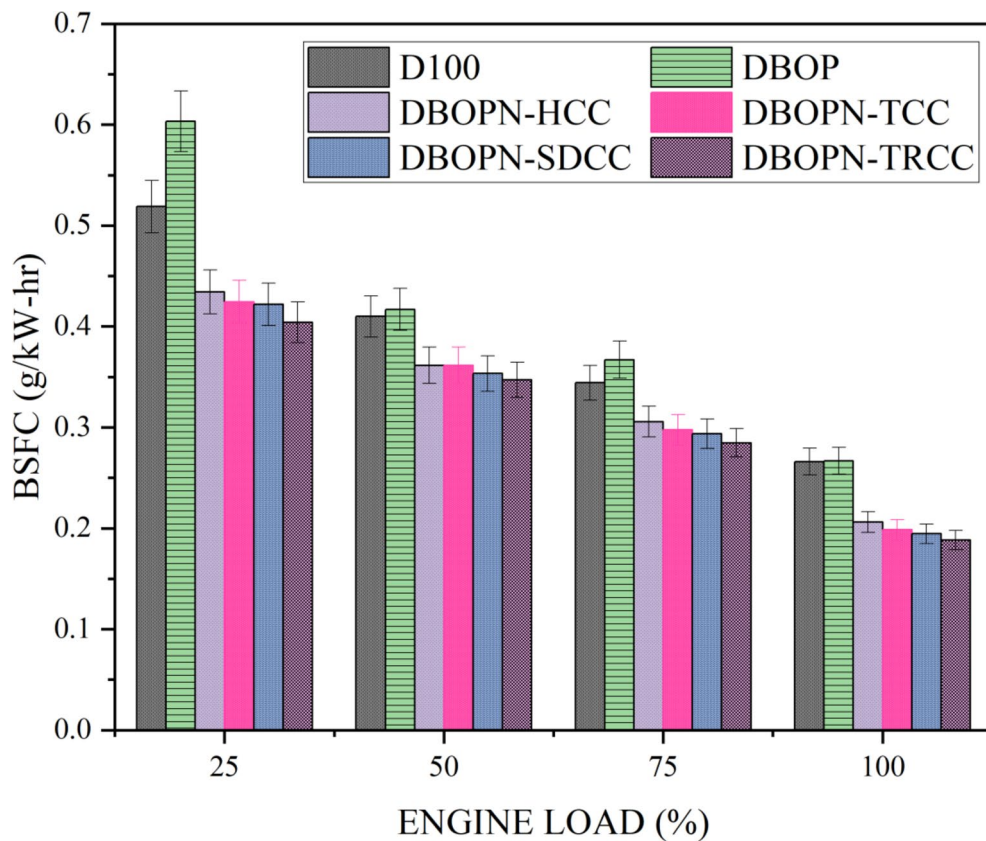


**Fig. 8.** Variation of BSFC with respect to engine load.

to lowered BTE due to abnormal fluctuation in swirl and turbulence resulting in reduced combustion efficiency followed by lowered BTE profile as reported such as Lalvani et al.<sup>64</sup>.

#### Emission characteristics

##### *Carbon monoxide (CO)*

The CO emission fluctuation for DBOPN in different piston bowl geometries with engine load is delineated in Fig. 10. From the figure, it is found that D100 emits more CO when compared to oxygenated additives since it has less built-in O<sub>2</sub> and can convert more easily into CO<sub>2</sub> during oxidation. All other geometries show lower CO emissions when compared to DBOPN-HCC. The CO emissions of DBOPN-TCC, DBOPN-SDCC, and DBOPN-TRCC are, at 100% engine load, approximately 48.85%, 5.96%, and 90.16% lower than those of DBOPN-HCC. The O<sub>2</sub> present in BBOPN mixes, which may have increased CO oxidation and thus reduced CO emission, and improved air circulation within the combustion chamber are responsible for this enormous reduction in CO emissions. Maximum CO reduction is evident for DBOPN-TCC and DBOPN-TRCC due to potential utilization of inbuilt O<sub>2</sub>, quick fuel molecule breaking and swirl improvement along with squish formation which causes the fuel to be directly concerned with the combustion chamber. Overall, DBOPN-TRCC results in reduced CO emission throughout the load. Reduced CO emission with such a re-entrant profile is confirmed with the results revealed by Wickman et al.<sup>40</sup> and Venkateswaran and Nagarajan<sup>67</sup>. With toroidal re-entrant bowl geometry, CO is found to increase in the literature of Benajes et al.<sup>68</sup>. However, some contradictory results with toroidal re-entrant bowl geometry giving rise to lowered CO were reported such as Mamilla et al.<sup>65</sup>, Li et al.<sup>20</sup>, Jaichandar and Annamalai<sup>63</sup>, Dolak et al.<sup>69</sup>, Lalvani et al.<sup>64</sup> and Venkateswaran and Nagarajan<sup>67</sup> which could be attributed to poor utilisation of inbuilt O<sub>2</sub>, difficulty in fuel molecule breaking and poor swirl development which causes the fuel to be poorly oxidized and reduced CO levels.

##### *HC (hydrocarbon)*

Figure 11 portrays the fluctuation of HC emission for DBOPN in different piston bowl geometries with engine loads. The deduction is that the alteration of the combustion chamber can significantly contribute to the reduction of Hydrocarbon (HC) emissions. HC emissions are highest for D100, while the lowest HC is reported for DBOPN-TRCC throughout the engine load condition. At 100% load, DBOPN-TRCC exhibits HC emission of about 0.02 g/kWh which is lower than DBOPN-HCC, DBOPN-TCC and DBOPN-SDCC by about 59.95%, 57.78% and 41.63% respectively. TRCC bowl supports the turbulent kinetic energy of the fuel mixture and therefore channels to the combustion zone. This occurrence, therefore, lowers the possibility of formation of fuel-rich zones followed by HC emission reduction. Even though DBOPN-TCC is comparatively lesser HC than DBOPN-HCC, the quantum of emissions is higher than other chambers such as SDRC and TRCC which could

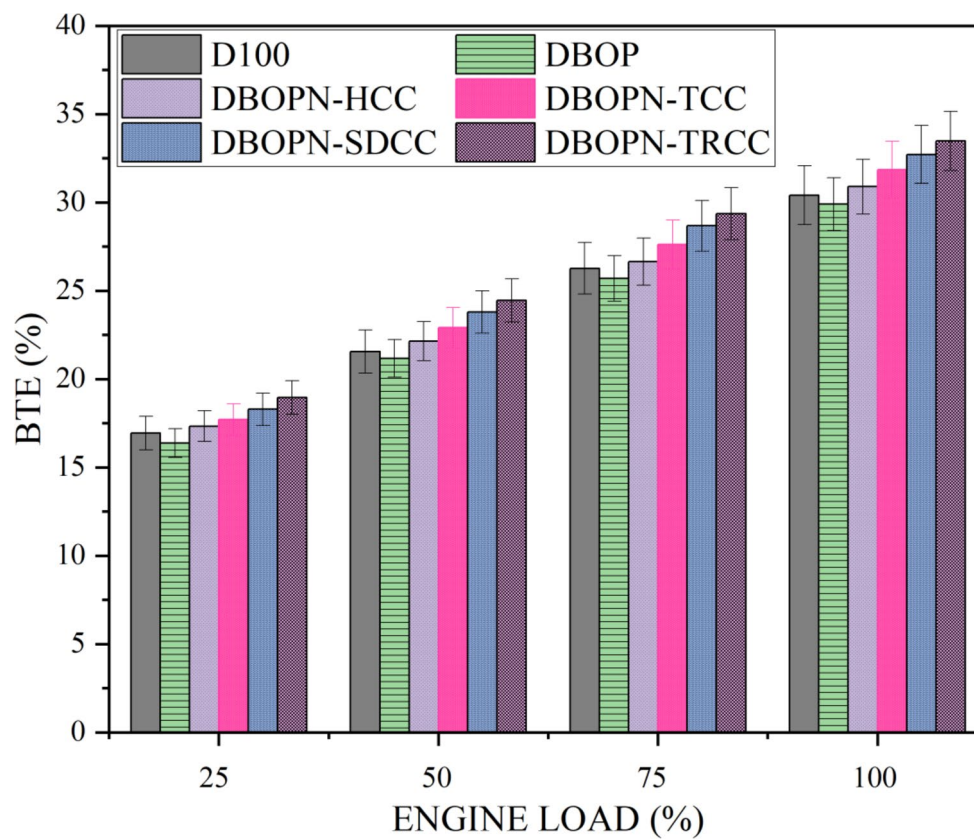


**Fig. 9.** Variation of BTE with respect to engine load.

be possibly attributed to TCC due to absence of re-entrant geometry causes wall wetting tendency followed by higher HC emission. The reduced Hydrocarbon (HC) emissions, particularly evident with the TRCC geometry, align closely with the research findings of Jaichandar et al.<sup>70</sup> and Wickman et al.<sup>40</sup>. With toroidal re-entrant bowl geometry, the HC emissions are found to increase in the literatures of Benajes et al.<sup>68</sup>. However, some contradictory results with toroidal re-entrant bowl geometry giving rise to lowered HC emissions were reported such as Mamilla et al.<sup>65</sup>, Lavani et al.<sup>64</sup> and Venkateswaran and Nagarajan<sup>67</sup> as a result of lowered rich mixture zones in crevice areas of the combustion chamber due to the presence of swirl in combustion chamber.

#### *NO<sub>x</sub> (oxides of nitrogen)*

NO<sub>x</sub> fluctuation for DBOPN with relation to engine load is shown in Fig. 12 for various combustion chamber designs. D100 is the mix that shows the least amount of NO<sub>x</sub> when the engine is running. At engine loads of 25%, 50%, 75%, and 100%, respectively, the NO<sub>x</sub> emissions of DBOPN-HCC were approximately 45.8%, 57.43%, 47.46%, and 57.18% higher than those of D100. When using a DBOPN mix, all of the four bowl geometries—TCC, SDRCC, and TRCC—show greater NO<sub>x</sub> levels than HCC. At 100% load, the NO<sub>x</sub> liberated by DBOPN-TCC, DBOPN-SDRCC and DBOPN-TRCC were about 17.56 g/kWh, 18.03 g/kWh and 18.81 g/kWh respectively, while DBOPN-HCC emits only 17.09 g/kWh. Consequently, the DBOPN-TCC configuration achieved the lowest NO<sub>x</sub> emissions due to reduced swirl and squish fuel motion. This directs the fuel spray away from the combustion zone, thereby lowering the adiabatic temperature and resulting in reduced NO<sub>x</sub> emissions. Higher NO<sub>x</sub> emissions of DBOPN-TRCC are merely compensated for improved BTE and the lowered CO, HC emissions with respect to other geometries. Higher NO<sub>x</sub> emissions with TRCC are reported by few researchers<sup>65,70</sup>.

While some contradiction results with lowered NO<sub>x</sub> with TRCC is also reported by Wei et al.<sup>71</sup>, Prasad et al.<sup>72</sup> and Wickman et al.<sup>40</sup>. With toroidal re-entrant bowl geometry, the NO<sub>x</sub> emissions are found to increase in the literatures of Mamilla et al.<sup>65</sup>, Jaichandar and Annamalai<sup>63,70</sup>, Li et al.<sup>20</sup>, Lavani et al.<sup>64</sup> and Venkateswaran and Nagarajan<sup>67</sup>. However, some contradictory results with toroidal re-entrant bowl geometry giving rise to lowered NO<sub>x</sub> emissions were reported such as Wickman et al.<sup>40</sup>, Lim and Min<sup>73</sup> and Wei et al.<sup>71</sup>. This can be attributed to a reduction in swirl and squish fuel motion, directing the fuel spray away from the combustion zone, thereby reduced adiabatic temperature and poor O<sub>2</sub> utilization lowering the NO<sub>x</sub> emission subsequently.

#### *Smoke opacity*

The fluctuation smoke opacity for DBOPN in various combustion chamber designs in relation to engine load is shown in Fig. 13. As most of the literature points out, it can be seen as a trade-off feature between smoke opacity and NO<sub>x</sub> emissions. For D100, the maximum smoke opacity is seen at all engine load conditions. When

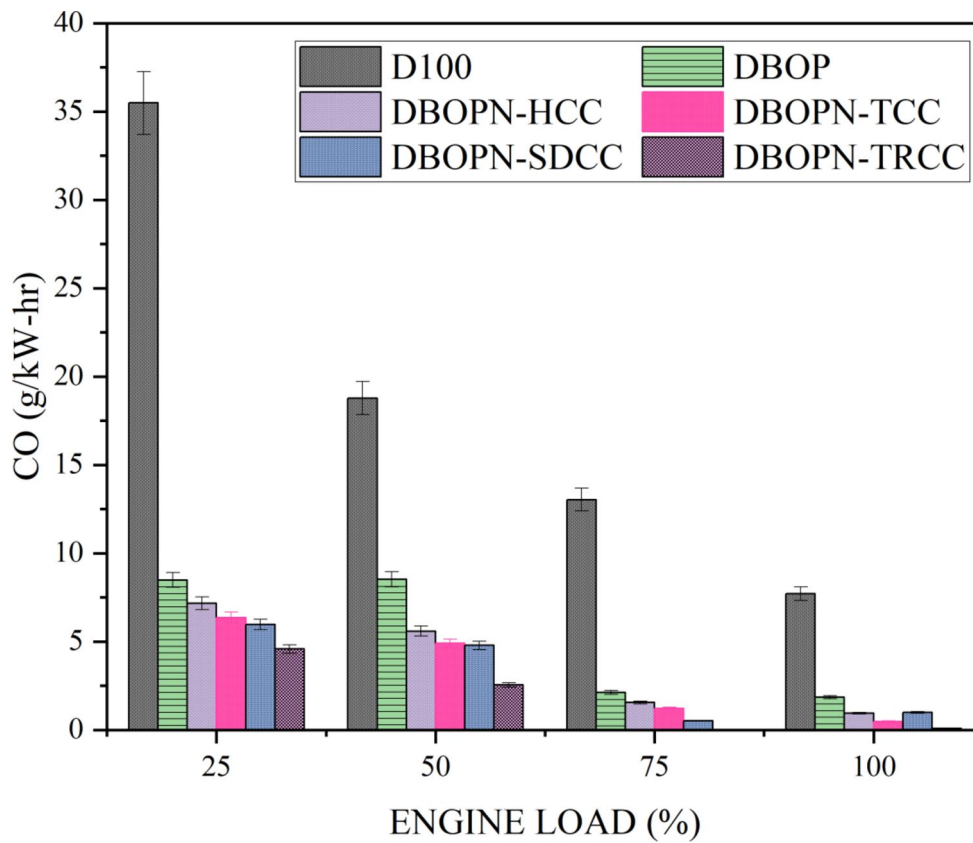


**Fig. 10.** Fluctuation in carbon monoxide (CO) levels in relation to engine load.

comparing DBOPN-TCC, DBOPN-SDCC, and DBOPN-TRCC to DBOPN-HCC, the smoke opacity of each is approximately 2.71%, 3.58%, and 15.48% lower, respectively, at 100% engine load. This can be attributed to the various bowl shapes that provide efficient spray penetration, enhanced evaporation, and rapid precursor burning, all of which reduce the likelihood of undesired fuel accumulation and the air shortfall in the combustion zone, giving rise to lowered smoke emissions. DBOPN-TRCC achieved highest smoke reduction throughout the load could be attributed to enhanced fuel swirl thereby lessening the soot precursor formation, improved oxidation followed by lowered smoke. Lowered smoke capacity with the usage of re-entrant bowl profile was on par with similar research findings of Wei et al.<sup>71</sup>. Results with toroidal re-entrant bowl geometry giving rise to lowered smoke emissions were reported such as Mamilla et al.<sup>65</sup>, Jaichandar and Annamalai<sup>63,70</sup>, Lalvani et al.<sup>64</sup> and Venkateswaran and Nagarajan<sup>67</sup> and Dolak et al.<sup>69</sup>.

#### LSTM algorithm prediction

The results have been included into the LSTM network to examine how various fuel mixes operate and what kind of emissions they produce under full engine load (80–100%) condition. To validate the model, the collected data is used for training and subsequently compared to the values generated by the LSTM network. For most parameters, a second-order function was applied to ensure consistency, and the dataset was constructed to encompass Brake Thermal Efficiency (BTE), Brake Specific Fuel Consumption (BSFC) and the concentrations of Carbon Dioxide ( $\text{CO}_2$ ), Carbon Monoxide (CO), Nitrogen Oxides (NOx), and smoke opacity. Table 11 presents the regression model coefficients (P, Q, R, S) associated with various parameters (BTE, BSFC, HC, CO, NOx and smoke opacity). In each case, coefficient P holds no significance. These regression coefficients are employed to prepare and subsequently train the dataset in conjunction with LSTM. Figures 14 and 15 have been included to depict the comparison of regression models with Long Short-Term Memory (LSTM) specifically for Brake Thermal Efficiency (BTE) and Hydrocarbon emissions (HC). Similarly, this methodology can be extended to predict various parameters. Table 12 displays the Root Mean Square Error (RMSE) values for the LSTM model concerning different parameters for the test fuels. Upon the obtained predicted data, LSTM could act as an effective tool for the present state of art problems. Also, LSTM can be effectively implemented in optimizing the sourced data from the diesel engine with lesser RMSE values.

#### Diesel RK—fuel spray visualization

The DBOP blend is a blend consisting of diesel/Jatropha biodiesel, vegetable oil and pentanol with different concentrations. To enhance its properties, it has been enriched with alumina nano additives at a concentration of 20 parts per million (ppm). The resulting fuel is referred to as DBOPN. Subsequently, the properties of HPF are utilized as inputs, which run over identical working environment to those of a typical diesel engine. The

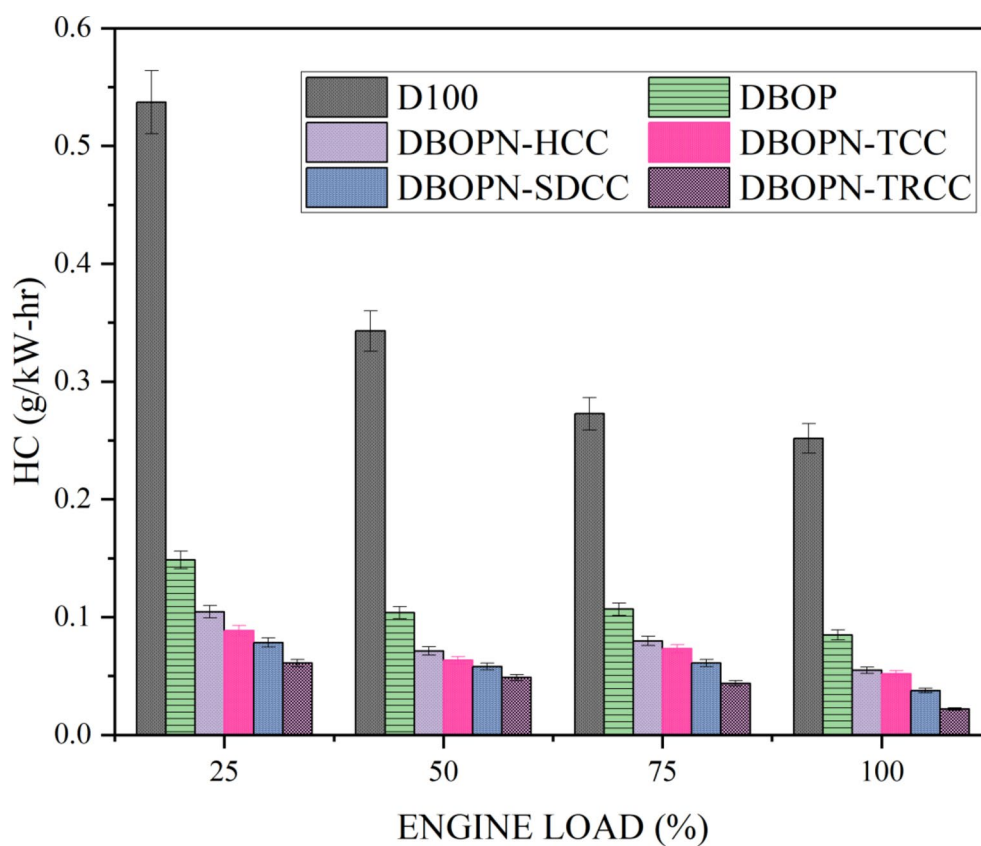


**Fig. 11.** Changes in hydrocarbon (HC) levels with engine load.

software analyzes the performance of the engine using different combustion chamber geometries, including HCC (Homogeneous Charge Compression), SDRCC (Swirl Direct Re-entrant Combustion Chamber), TCC (Turbulence Charge Compression), and TRCC (Toroidal Re-entrant Combustion Chamber). The simulation within Diesel-RK focuses on fuel spray occurrence and combustion phenomenon within the various bowl profiles, as illustrated in Fig. 16. Among these geometries, the TRCC design stands out as the most effective in terms of enhancing performance and optimizing combustion parameters. This superiority is attributed to the TRCC's ability to generate a potent squish effect along with efficient air movement, resulting in improved air-fuel interaction.

The outcomes derived from the Diesel-RK simulation are compared with actual experimental data obtained under identical operating conditions. The comparison involves the utilization of DBOPN blend and various bowl strategies. Table 13 presents the comparative analysis of these results. It is evident that the TRCC geometry consistently outperforms the other combustion chamber designs in several key aspects, including BTE, BSFC, higher  $P_{cyl}$ , and an increased HRR. This excellence is mainly credited to the generated squish effect and swirled air movement within the TRCC design, which significantly contributes to turbulence generation and, consequently, enhances the combustion efficiency. Notably, the simulation outcomes are closely aligned with the experimental values, underscoring the accuracy of the Diesel-RK software in predicting engine performance. However, it should be noted that the theoretical simulation values tend to be slightly higher than the actual values due to the omission of factors such as heat losses and friction in the simulation model. In a related study, Al-Dawody and Bhatti<sup>60</sup> conducted a thorough investigation using the DIESEL-RK simulation software to optimize strategies for reducing nitrogen oxide (NOx) emissions in diesel engines. Their findings highlighted that a deeper piston bowl with a smaller diameter had a significant mitigating effect on NOx emissions. Similar reports were reported by Kuleshov<sup>61</sup> with modified piston bowl having the greater turbulence shown higher performance of the diesel engine.

## Conclusion

The present work explores the integration of nanotechnology and Long Short-Term Memory (LSTM) machine learning algorithms to enhance the understanding and optimization of fuel spray dynamics in compression ignition (CI) engines with varying bowl geometries.

- The test fuel used is a quaternary fuel (50% diesel (vol%) + 5% biodiesel (vol%) + 5% vegetable oil (vol%) + 40% (vol%) pentanol) with various combustion bowl strategies such as hemispherical, toroidal, shallow depth and toroidal re-entrant chambers.

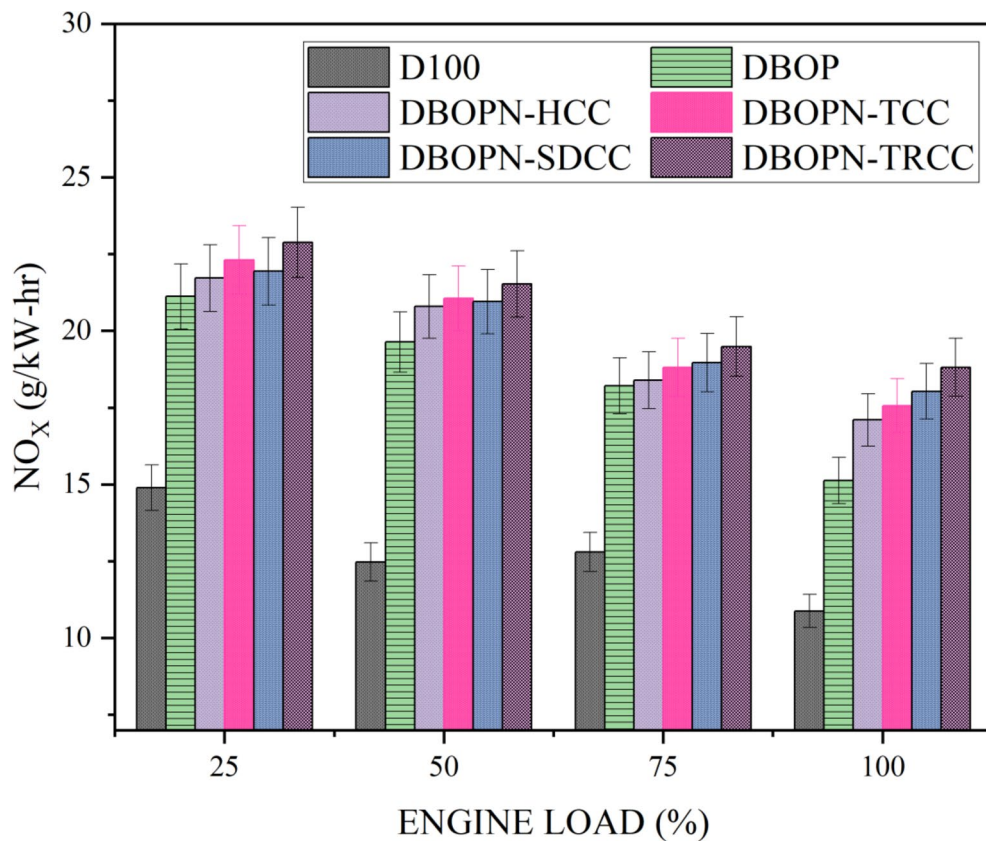


**Fig. 12.** Changes in nitrogen oxide (NO<sub>x</sub>) levels in correlation with engine load.

- DBOPN-TRCC is found to exhibit 8.13% higher BTE and 8.65% lowered BSFC than the conventional HCC bowl. DBOPN-TRCC is found to have 90.16% lowered CO, 59.95% lowered HC and 15.48% lowered smoke owing to improved spray penetration and faster burning of soot precursors. However, NO<sub>x</sub> emissions of DBOPN-TRCC were found to be higher (by 10.01% in comparison with DBOPN-HCC at full load). Overall, DBOPN-TRCC blend is found to have improved performance and minimized emission characteristics.
- The outcomes were trained and validated using LSTM networks. The regression coefficients indicate that the LSTM approach is effective in predicting both performance and emissions across a wide range of loading conditions. Application of toroidal re-entrant bowl geometry (TRCC) in quaternary fuel could be regarded as a promising substitute for traditional fossil fuels. Diesel-RK results also highlighted that a deeper piston bowl with a smaller diameter had a significant mitigating effect on NO<sub>x</sub> emissions<sup>74</sup>.

#### Scope for future work

The work can be extended to study the behavior of gaseous fuels or dual fuels with different combustion geometries. Also, microscopic analysis of fuel spray with photographs can be an interesting add on to the existing work.

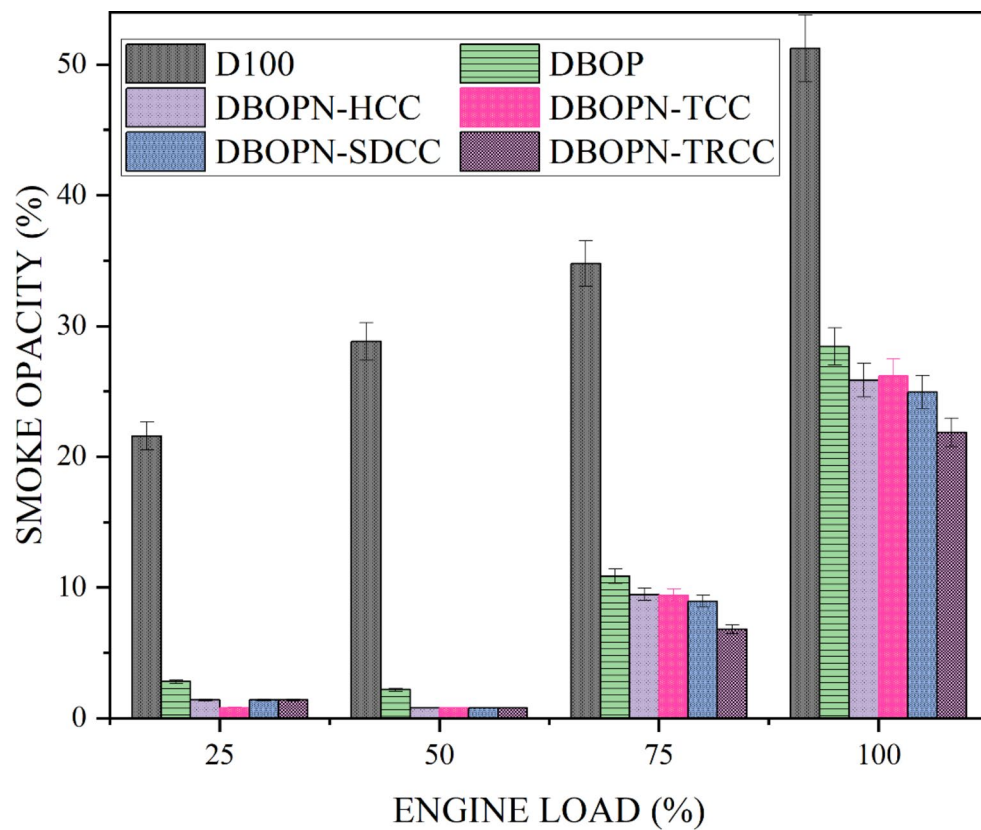


**Fig. 13.** Variation of smoke opacity with respect to engine load.

	<b>P</b>	<b>Q</b>	<b>R</b>	<b>S</b>
<b>Brake thermal efficiency (BTE)</b>				
D100	–	– 0.0036	0.563	– 0.398
DBOP	–	– 0.0034	0.576	– 0.248
DBOPN-HCC	–	– 0.0034	0.521	0.132
DBOPN-TCC	–	– 0.0036	0.546	– 0.692
DBOPN-SDCC	–	– 0.0037	0.535	– 1.286
DBOPN-TRCC	–	– 0.0038	0.562	– 2.323
<b>Brake specific fuel consumption (BSFC)</b>				
D100	–	0.004	– 0.002	0.4965
DBOP	– 6E-04	0.003	– 0.001	0.4762
DBOPN-HCC	– 7E-05	0.0002	– 0.0132	0.5376
DBOPN-TCC	– 6E-04	0.005	– 0.0142	0.7826
DBOPN-SDCC	– 7E-05	0.0001	– 0.0039	1.0236
DBOPN-TRCC	– 2E-06	0.0004	0.0287	0.9876
<b>Hydrocarbon (HC)</b>				
D100	–	0	0.324	26.72
DBOP	–	– 0.002	0.420	20.58
DBOPN-HCC	–	– 0.002	0.396	19.54
DBOPN-TCC	–	– 0.003	0.487	16.23
DBOPN-SDCC	–	– 0.002	0.212	18.76
DBOPN-TRCC	–	0	0.218	18.25
<b>Carbon monoxide (CO)</b>				
D100	–	0.0004	– 0.002	0.420
DBOP	–	0.00005	– 0.003	0.262
DBOPN-HCC	–	0.00004	– 0.002	0.136
DBOPN-TCC	–	0.00005	– 0.003	0.072
DBOPN-SDCC	–	0.00006	– 0.004	0.007
DBOPN-TRCC	–	0.00006	– 0.005	– 0.326
<b>Nitrogen oxide (<math>\text{NO}_x</math>)</b>				
D100	–	0.006	4.926	1.93
DBOP	–	– 0.0034	0.7324	– 0.0523
DBOPN-HCC	–	– 0.0034	0.7124	1.8612
DBOPN-TCC	–	– 0.0036	0.755	– 1.5362
DBOPN-SDCC	–	– 0.0037	0.7682	– 1.2842
DBOPN-TRCC	–	– 0.0038	0.7684	– 3.2632
<b>Smoke opacity</b>				
D100	–	0.025	0.0023	0.146
DBOP	–	0.036	0.0024	0.162
DBOPN-HCC	–	0.042	0.0023	0.243
DBOPN-TCC	–	0.078	0.0046	0.026
DBOPN-SDCC	–	0.023	0.0023	– 0.126
DBOPN-TRCC	–	0.053	0.0046	– 0.643

**Table 11.** Aggression model coefficients for various test parameters.

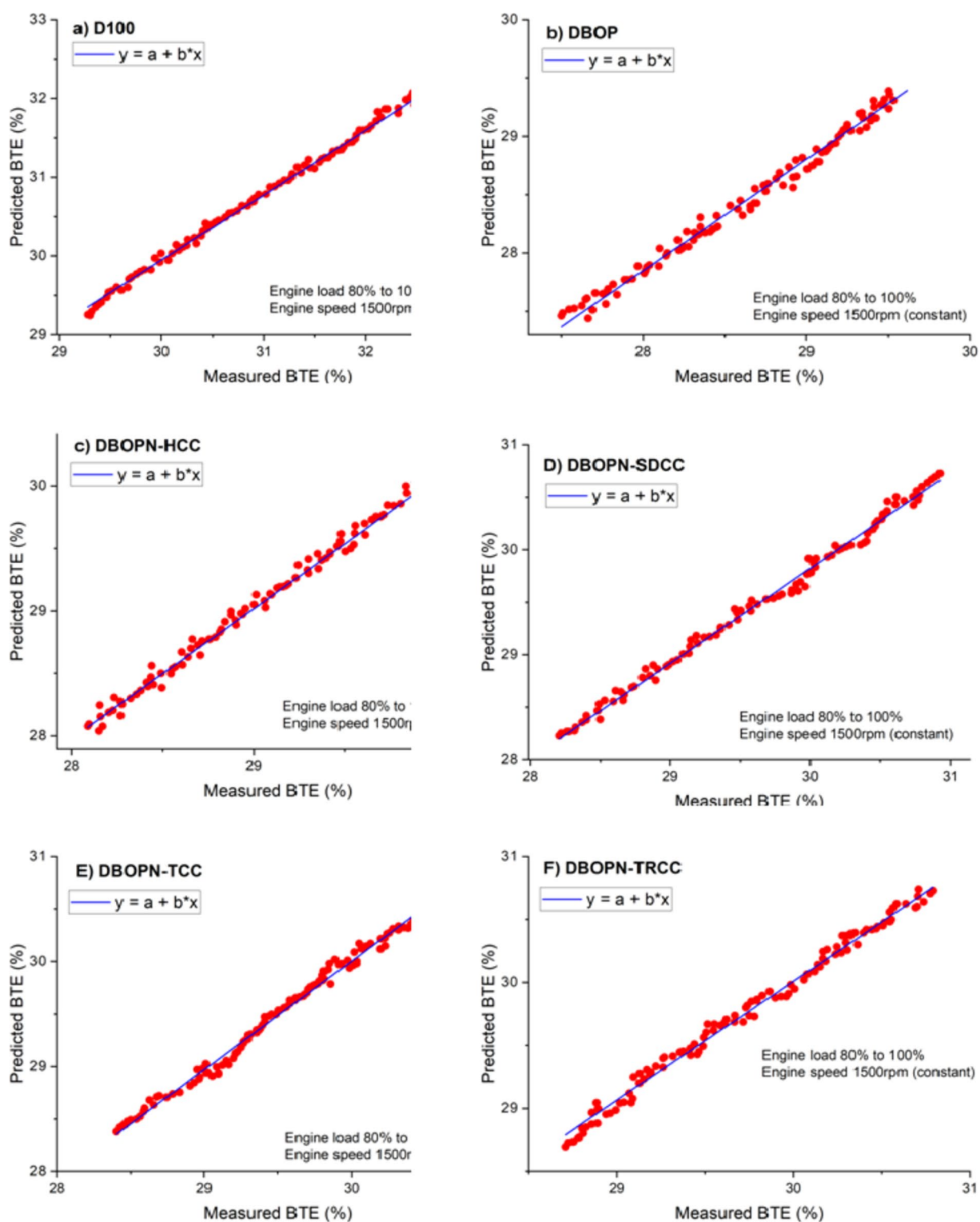


**Fig. 14.** Prediction verses measured BTE for LSTM machine learning model.

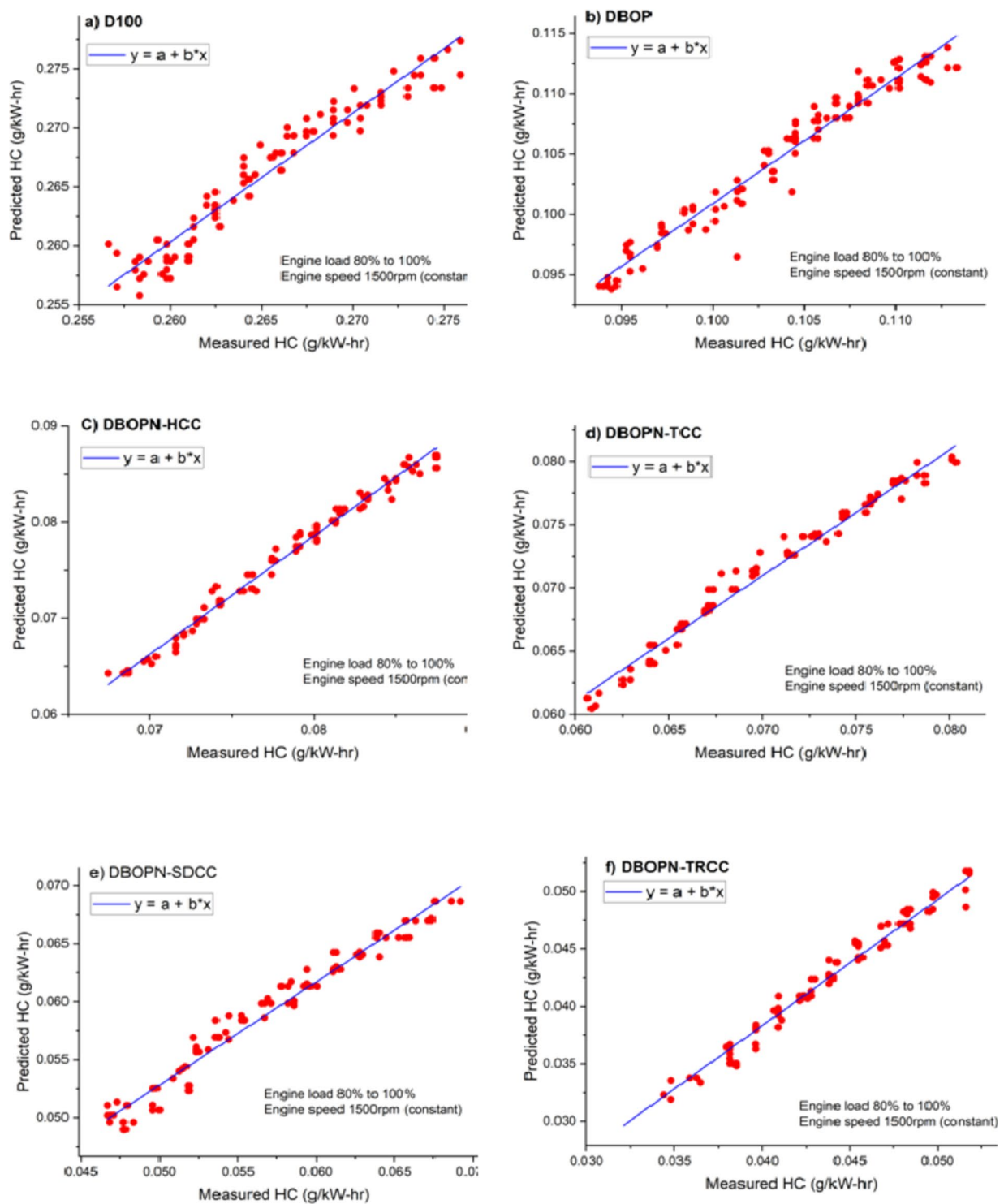


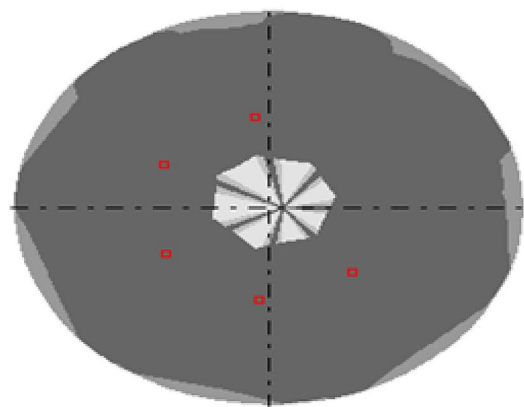
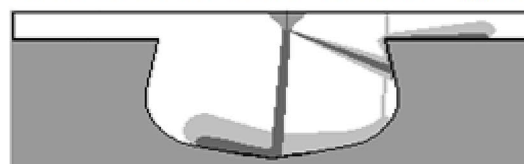
**Fig. 15.** Prediction versus measured HC for LSTM machine learning model.

Fuel/parameter	BTE	BSFC	HC	CO	NO <sub>x</sub>	Smoke opacity
D100	0.0632	0.01736	0.5234	0.0143	6.3215	0.1304
DBOP	0.02872	6.00412	0.1642	0.0173	6.7432	0.1835
DBOPN-HCC	0.25983	0.01376	0.1082	0.01918	8.0423	0.1202
DBOPN-TCC	0.02981	0.01683	0.1932	0.01326	10.546	0.1504
DBOPN-SDCC	0.01863	0.02345	0.2962	0.0075	11.236	0.0986
DBOPN-TRCC	0.07432	0.00242	0.3214	0.0072	13.2695	0.0278

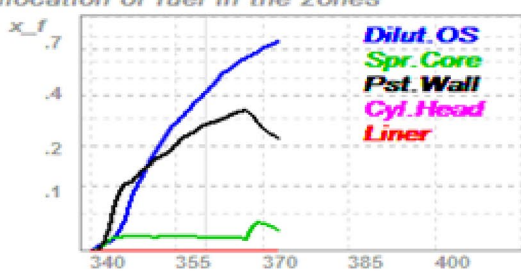
**Table 12.** Root mean square error (RMSE) values for the LSTM model.

The results of diesel mixture formation and combustion simulation  
2023-09-27 06-40-13 "1L8.8/11" ||| Mode: #1 :: "RPM=1500"

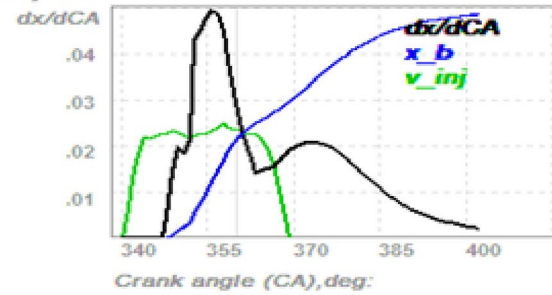
HCC



Allocation of fuel in the zones

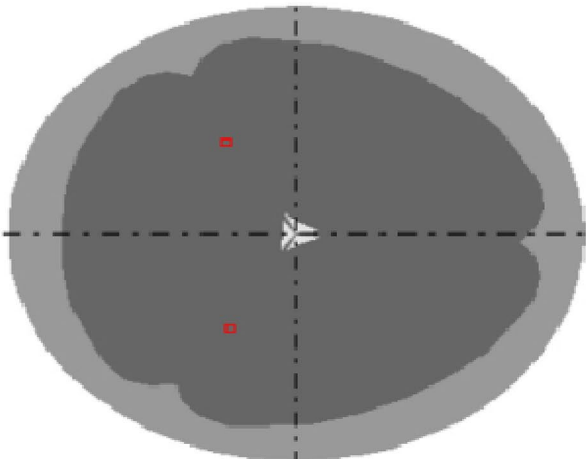
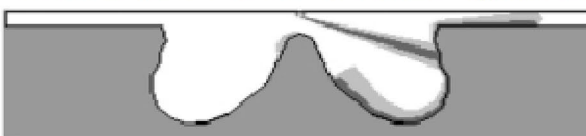


Injection and heat release

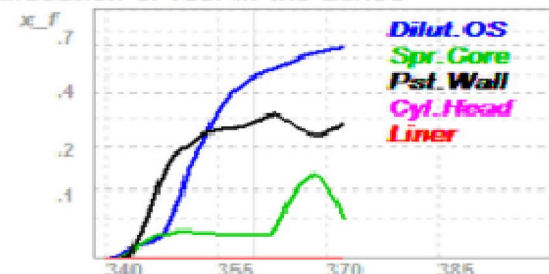


The results of diesel mixture formation and combustion simulation  
2019-01-16 22-49-29 "1L8.8/11" ||| Mode: #1 :: "RPM=1500"

TRCC



Allocation of fuel in the zones



Injection and heat release

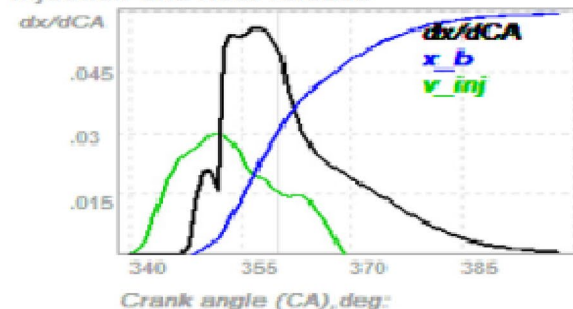
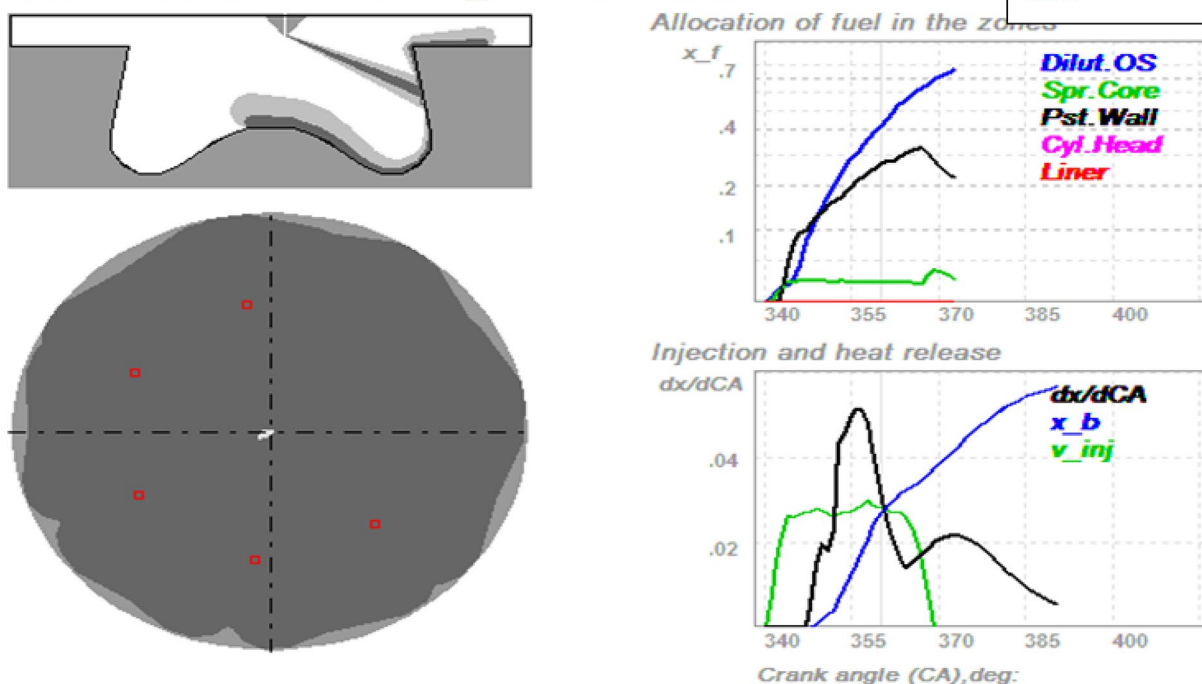


**Fig. 16.** Simulation of fuel spray formation and combustion for different bowl geometries.

The results of diesel mixture formation and combustion simulation  
 2023-09-27 07-02-25 "1L8.8/11" ||| Mode: #1 :: "RPM=1500"



The results of diesel mixture formation and combustion simulation  
 2023-09-27 06-33-10 "1L8.8/11" ||| Mode: #1 :: "RPM=1500"

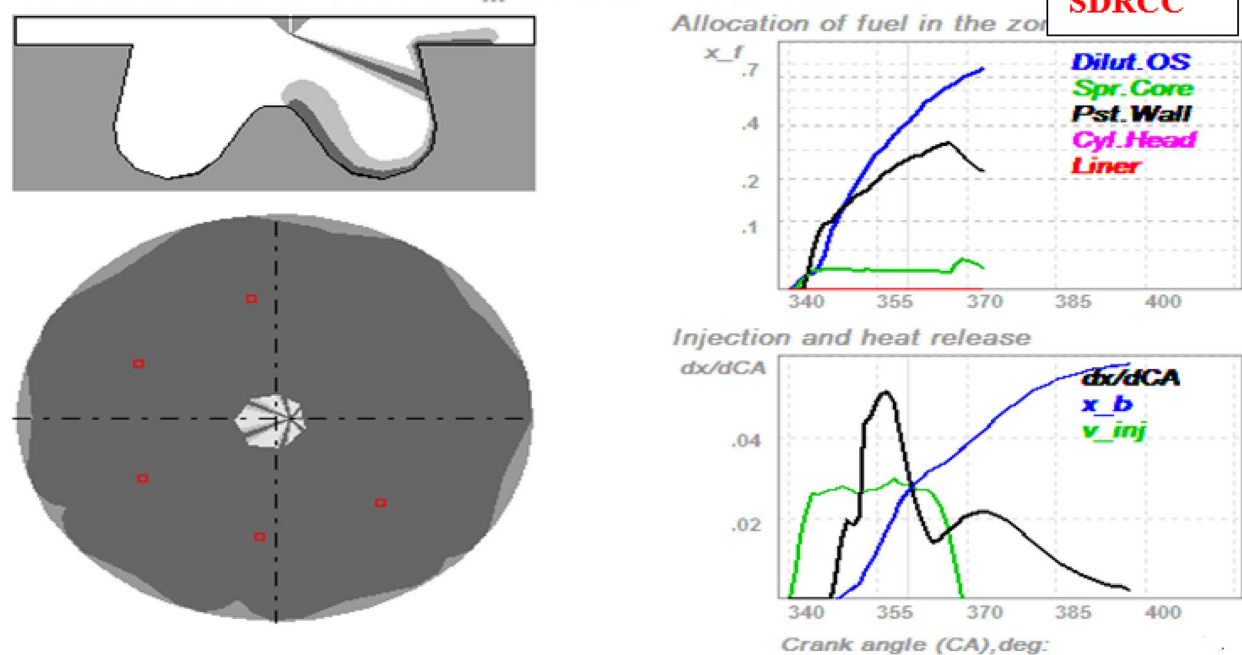


**Figure 16.** (continued)

Combustion chamber	BTE (%)		BSFC (g/kWh)		HC (g/kW-h)		CO (g/kW-h)		NO <sub>x</sub> (g/kW-h)	
	(a)	(b)	(a)	(b)	(a)	(b)	(a)	(b)	(a)	(b)
HCC	30.51	30.2781	0.20619	0.2134	0.05483	0.0489	0.93991	0.9541	17.0991	17.234
SDRCC	31.0012	31.1543	0.19459	0.1902	0.03762	0.0396	0.98388	0.9432	18.0315	18.156
TCC	30.7498	30.9623	0.19848	0.1876	0.05201	0.0497	0.48074	0.5019	17.5628	17.6285
TRCC	31.3020	31.5962	0.18836	0.1854	0.02196	0.0198	0.08686	0.0791	18.8145	18.203

**Table 13.** Synopsis of (a) test results and (b) Diesel-RK simulation findings of CI engine with DBOPN.

## Data availability

The datasets used and/or analysed during the current study available from the corresponding author on reasonable request.

Received: 25 July 2024; Accepted: 12 December 2024

Published online: 06 January 2025

## References

- Mei, Q., Liu, L., Yang, W. & Tang, Y. Combustion model development of future DI engines for carbon emission reduction. *Energy Convers. Manag.* **311**, 118528 (2024).
- Azeez, O. S. et al. Modeling of CO emissions from traffic vehicles using artificial neural networks. *Appl. Sci.* **9**(2), 313 (2019).
- Özener, O., Yüksek, L. & Özkan, M. Artificial neural network approach to predicting engine-out emissions and performance parameters of a turbo charged diesel engine. *Therm. Sci.* **17** (1), 153–166 (2013).
- Roy, S., Banerjee, R., Das, A. K. & Bose, P. K. Development of an ANN based system identification tool to estimate the performance-emission characteristics of a CRDI assisted CNG dual fuel diesel engine. *J. Nat. Gas Sci. Eng.* **21**, 147–158 (2014).
- Rai, A. A., Pai, P. S. & Rao, B. S. Prediction models for performance and emissions of a dual fuel CI engine using ANFIS. *Sadhana* **40** (2), 515–535 (2015).
- Deniz, S., Gökçen, H. A. D. İ. & Nakhaeizadeh, G. Application of data mining methods for analyzing fuel consumption and emission levels. *Int. J. Eng. Res. Technol.* **5** (10), 1 (2016).
- Uşlu, S. & Celik, M. B. Performance and exhaust emission prediction of a SI engine fueled with I-amyl alcohol-gasoline blends: an ANN coupled RSM based optimization. *Fuel* **265**, 116922 (2020).
- Lu, G. et al. High performance mixed-potential type NO<sub>x</sub> sensor based on stabilized zirconia and oxide electrode. *Solid State Ion.* **262**, 292–297 (2014).
- Nishio, Y., Murata, Y., Yamaya, Y. & Kikuchi, M. Optimal calibration scheme for map-based control of diesel engines. *Sci. China Inf. Sci.* **61** (7), 70205 (2018).
- Kurzydym, D., Źmudka, Z., Perrone, D. & Klimanek, A. Experimental and numerical investigation of nitrogen oxides reduction in diesel engine selective catalytic reduction system. *Fuel* **313**, 122971 (2022).
- Veza, I. et al. Review of artificial neural networks for gasoline, diesel and homogeneous charge compression ignition engine. *Alexand. Eng. J.* **61** (11), 8363–8391 (2022).
- Ragaller, P. et al. *Particulate Filter Soot Load Measurements Using Radio Frequency Sensors and Potential for Improved Filter Management* (No. 2016-01-0943). SAE Technical Paper (2016).
- Liu, B., Hu, J., Yan, F., Turkson, R. F. & Lin, F. A novel optimal support vector machine ensemble model for NO<sub>x</sub> emissions prediction of a diesel engine. *Measurement* **92**, 183–192 (2016).
- Jiang, K., Cao, E. & Wei, L. NO<sub>x</sub> sensor ammonia cross-sensitivity estimation with adaptive unscented Kalman filter for Diesel-engine selective catalytic reduction systems. *Fuel* **165**, 185–192 (2016).
- Shin, S. et al. Designing a steady-state experimental dataset for predicting transient NO<sub>x</sub> emissions of diesel engines via deep learning. *Expert Syst. Appl.* **198**, 116919 (2022).
- Feizizadeh, B., Omarzadeh, D., Kazemi Garajeh, M., Lakes, T. & Blaschke, T. Machine learning data-driven approaches for land use/cover mapping and trend analysis using Google Earth Engine. *J. Environ. Plann. Manag.* **66** (3), 665–697 (2023).
- Planakis, N., Papalambrou, G., Kyrtatos, N. & Dimitrakopoulos, P. *Recurrent and Time-Delay Neural Networks as Virtual Sensors for NOx Emissions in Marine Diesel Powertrains* (No. 2021-01-5042). SAE Technical Paper (2021).
- Shin, S. et al. Deep neural network model with Bayesian hyperparameter optimization for prediction of NO<sub>x</sub> at transient conditions in a diesel engine. *Eng. Appl. Artif. Intell.* **94**, 103761 (2020).
- Yurtseven, E., Lambert, J., Carballo, A. & Takeda, K. A survey of autonomous driving: Common practices and emerging technologies. *IEEE Access* **8**, 58443–58469 (2020).
- Li, J., Yang, W. M., An, H., Maghbouli, A. & Chou, S. K. Effects of piston bowl geometry on combustion and emission characteristics of biodiesel fueled diesel engines. *Fuel* **120**, 66–73 (2014).
- Hirschberg, J. & Manning, C. D. Advances in natural language processing. *Science* **349** (6245), 261–266 (2015).
- Cambria, E. & White, B. Jumping NLP curves: A review of research in natural language processing. *IEEE Comput. Intell. Mag.* **9** (2), 48–57 (2014).
- Wang, M. & Deng, W. Deep face recognition: A survey. *Neurocomputing* **429**, 215–244 (2021).
- Razali, N. A. M. et al. Gap, techniques and evaluation: traffic flow prediction using machine learning and deep learning. *J. Big Data* **8** (1), 1–25 (2021).
- Ramteke, S. M., Chelladurai, H. & Amarnath, M. Diagnosis and classification of diesel engine components faults using time-frequency and machine learning approach. *J. Vib. Eng. Technol.* **10** (1), 175–192 (2022).
- Atkinson, C. M., Long, T. W. & Hanzevack, E. L. *Virtual Sensing: A Neural Network-Based Intelligent Performance and Emissions Prediction System for On-Board Diagnostics and Engine Control* (No. 980516). SAE Technical Paper (1998).
- Traver, M. L., Atkinson, R. J. & Atkinson, C. M. *Neural Network-Based Diesel Engine Emissions Prediction Using In-Cylinder Combustion Pressure*. SAE Transactions 1166–1180 (1999).
- He, Y. & Rutland, C. J. Application of artificial neural networks in engine modelling. *Int. J. Engine Res.* **5** (4), 281–296 (2004).
- Arsie, I., Marrà, D., Pianese, C. & Sorrentino, M. Real-time estimation of engine NO<sub>x</sub> emissions via recurrent neural networks. *IFAC Proc. Vol.* **43** (7), 228–233 (2010).
- Alcan, G. et al. Predicting NO<sub>x</sub> emissions in diesel engines via sigmoid NARX models using a new experiment design for combustion identification. *Measurement* **137**, 71–81 (2019).

31. Yu, Y. et al. A novel deep learning approach to predict the instantaneous NO<sub>2</sub> emissions from diesel engine. *IEEE Access* **9**, 11002–11013 (2021).
32. Van Hung, T., Alkhamis, H. H., Alrefaei, A. F., Sohret, Y. & Brindhadevi, K. Prediction of emission characteristics of a diesel engine using experimental and artificial neural networks. *Appl. Nanosci.* **1**, 1–10 (2021).
33. Xie, H. et al. Parallel attention-based LSTM for building a prediction model of vehicle emissions using PEMS and OBD. *Measurement* **185**, 110074 (2021).
34. Castresana, J., Gabiña, G., Martin, L., Basterretxea, A. & Uriondo, Z. Marine diesel engine ANN modelling with multiple output for complete engine performance map. *Fuel* **319**, 123873 (2022).
35. Saito, T., Daisho, Y., Uchida, N. & Ikeya, N. *Effects of Combustion Chamber Geometry on Diesel Combustion*. SAE Transactions 793–803 (1986).
36. Zhu, Y., Zhao, H., Melas, D. A. & Ladommato, N. *Computational Study of the Effects of the Re-entrant Lip Shape and Toroidal Radii of Piston Bowl on a HSDI Diesel Engine's Performance and Emissions* (No. 2004-01-0118). SAE Technical Paper (2004).
37. Dolak, J. G., Shi, Y. & Reitz, R. D. *A Computational Investigation of Stepped-Bowl Piston Geometry for a Light Duty Engine Operating at Low Load* (2010-01-1263). SAE Technical Paper (2010).
38. Lim, J. & Min, K. *The Effects of Spray Angle and Piston Bowl Shape on Diesel Engine Soot Emissions Using 3-D CFD Simulation* (No. 2005-01-2117). SAE Technical Paper (2005).
39. Shi, Y. & Reitz, R. D. Optimization study of the effects of bowl geometry, spray targeting, and swirl ratio for a heavy-duty diesel engine operated at low and high load. *Int. J. Engine Res.* **9** (4), 325–346 (2008).
40. Wickman, D. D., Yun, H. & Reitz, R. D. *Split-Spray Piston Geometry Optimized for HSDI Diesel Engine Combustion*. SAE Transactions 488–507 (2003).
41. Sivakumar, M., Sundaram, N. S. & Thastagir, M. H. S. Effect of aluminium oxide nanoparticles blended pongamia methyl ester on performance, combustion and emission characteristics of diesel engine. *Renew. Energy* **116**, 518–526 (2018).
42. Ranjan, A. et al. Experimental investigation on effect of MgO nanoparticles on cold flow properties, performance, emission and combustion characteristics of waste cooking oil biodiesel. *Fuel* **220**, 780–791 (2018).
43. Mehregan, M. & Moghiman, M. Effects of nano-additives on pollutants emission and engine performance in a urea-SCR equipped diesel engine fueled with blended-biodiesels. *Fuel* **222**, 402–406 (2018).
44. El-Seesy, A. I., Attia, A. M. & El-Batsh, H. M. The effect of Aluminum oxide nanoparticles addition with Jojoba methyl ester-diesel fuel blend on a diesel engine performance, combustion and emission characteristics. *Fuel* **224**, 147–166 (2018).
45. Hoseini, S. S. et al. Novel environmentally friendly fuel: The effects of nanographene oxide additives on the performance and emission characteristics of diesel engines fuelled with *Ailanthus altissima* biodiesel. *Renew. Energy* **125**, 283–294 (2018).
46. Kumar, S., Dinesha, P. & Bran, I. Influence of nanoparticles on the performance and emission characteristics of a biodiesel fuelled engine: an experimental analysis. *Energy* **140**, 98–105 (2017).
47. Ashok, B., Nanthagopal, K., Mohan, A., Johny, A. & Tamilarasu, A. Comparative analysis on the effect of zinc oxide and ethanox as additives with biodiesel in CI engine. *Energy* **140**, 352–364 (2017).
48. Das, M., Sarkar, M., Datta, A. & Santra, A. K. Study on viscosity and surface tension properties of biodiesel-diesel blends and their effects on spray parameters for CI engines. *Fuel* **220**, 769–779 (2018).
49. Liu, Y. et al. Spray characteristics of biodiesel-polyoxymethylene dimethyl ethers (PODE) blends in a constant volume chamber. *Combust. Sci. Technol.* **195** (16), 4069–4091 (2023).
50. Chaudhari, V. D., Kulkarni, A. & Deshmukh, D. Spray characteristics of biofuels for advance combustion engines. *Clean. Eng. Technol.* **5**, 100265 (2021).
51. Park, S. H., Suh, H. K. & Lee, C. S. Effect of bioethanol–biodiesel blending ratio on fuel spray behavior and atomization characteristics. *Energy Fuels* **23** (8), 4092–4098 (2009).
52. Geng, L., Wang, Y., Wang, Y. & Li, H. Effect of the injection pressure and orifice diameter on the spray characteristics of biodiesel. *J. Traffic Transp. Eng. (English Ed.)* **7** (3), 331–339 (2020).
53. Li, F. et al. Comparison of macroscopic spray characteristics between biodiesel-pentanol blends and diesel. *Exp. Thermal Fluid Sci.* **98**, 523–533 (2018).
54. Zhang, P. et al. Spray, atomization and combustion characteristics of oxygenated fuels in a constant volume bomb: A review. *J. Traffic Transp. Eng. (English Ed.)* **7** (3), 282–297 (2020).
55. Raghu, P., Thilagan, K., Thirumoorthy, M., Lokachari, S. & Nallusamy, N. Spray characteristics of diesel and biodiesel in direct injection diesel engine. *Adv. Mater. Res.* **768**, 173–179 (2013).
56. Appavu, P. & Venu, H. Quaternary blends of diesel/biodiesel/vegetable oil/pentanol as a potential alternative feedstock for existing unmodified diesel engine: Performance, combustion and emission characteristics. *Energy* **186**, 115856 (2019).
57. Venu, H., Subramani, L. & Raju, V. D. Emission reduction in a DI diesel engine using exhaust gas recirculation (EGR) of palm biodiesel blended with TiO<sub>2</sub> nano additives. *Renew. Energy* **140**, 245–263 (2019).
58. Venu, H., Raju, V. D. & Subramani, L. Combined effect of influence of nano additives, combustion chamber geometry and injection timing in a DI diesel engine fuelled with ternary (diesel-biodiesel-ethanol) blends. *Energy* **174**, 386–406 (2019).
59. Liu, Y. et al. Machine learning based predictive modelling of micro gas turbine engine fuelled with microalgae blends on using LSTM networks: An experimental approach. *Fuel* **322**, 124183 (2022).
60. Al-Dawody, M. F. & Bhatti, S. K. Optimization strategies for mitigating the biodiesel NO<sub>x</sub> effect in diesel engines with experimental verification. *Energy. Convers. Manag.* **68**, 96–104. <https://doi.org/10.1016/j.enconman.2012.12.025> (2013).
61. Kuleshov, A. & Multi-Zone DI Diesel Spray Combustion Model and Its Application for Aligning Injector Design with Piston Bowl Shape. SAE Technical Paper 2007-01-1908. <https://doi.org/10.4271/2007-01-1908> (2007).
62. Venu, H., Raju, D., Subramani, L. & V and Combined effect of influence of nano additives, combustion chamber geometry and injection timing in a DI diesel engine fuelled with ternary (diesel-biodiesel-ethanol) blends. *Energy* **174**, 386–406. <https://doi.org/10.1016/j.energy.2019.02.163> (2019).
63. Jaichandar, S. & Annamalai, K. Effects of open combustion chamber geometries on the performance of pongamia biodiesel in a DI diesel engine. *Fuel* **98**, 272–279 (2012).
64. Lalvani, J. I. J., Parthasarathy, M., Dhinesh, B. & Annamalai, K. Pooled effect of injection pressure and turbulence inducer piston on performance, combustion, and emission characteristics of a DI diesel engine powered with biodiesel blend. *Ecotoxicol. Environ. Saf.* **134**, 336–343 (2016).
65. Mamilla, V. R. et al. Effect of combustion chamber design on a DI diesel engine fuelled with jatropha methyl esters blends with diesel. *Procedia Eng.* **64**, 479–490 (2017).
66. Bapu, B. R., Saravanakumar, L. & Prasad, B. D. Effects of combustion chamber geometry on combustion characteristics of a DI diesel engine fueled with CalophyllumInophyllum methyl ester. *J. Energy Inst.* **90** (1), 82–100 (2017).
67. Venkateswaran, S. P. & Nagarajan, G. Effects of the re-entrant bowl geometry on a DI turbocharged diesel engine performance and emissions—a CFD approach. *J. Eng. Gas Turbines Power* **132**, 12 (2010).
68. Benajes, J., Pastor, J. V., Garcia, A. & Monsalve-Serrano, J. An experimental investigation on the impact of piston bowl geometry on RCCI performance and emissions in a heavy-duty engine. *Energy. Convers. Manag.* **103**, 1019–1030 (2015).
69. Dolak, J. G., Shi, Y. & Reitz, R. D. *A Computational Investigation of Stepped-Bowl Piston Geometry for a Light-Duty Engine Operating at Low Load*. SAE Technical Paper, No. 2010-01-1263 (2010).
70. Jaichandar, S., Kumar, P. S. & Annamalai, K. Combined impact of injection timing and combustion chamber geometry on the performance of a biodiesel-fueled diesel engine. *Energy* **47**, 388–394 (2012).

71. Wei, S., Wang, F., Leng, X., Liu, X. & Ji, K. Numerical analysis on the effect of swirl ratios on swirl chamber combustion system of DI diesel engines. *Energy Convers. Manag.* **75**, 184–190 (2013).
72. Prasad, B. V. S. U., Sharma, C. S., Anand, T. N. C. & Ravikrishna, R. V. High swirl-inducing piston bowls in small diesel engines for emission reduction. *Appl. Energy* **88**, 2355–2367 (2011).
73. Lim, J. & Min, K. *The Impact of Spray Angle and Piston Bowl Shape on Diesel Engine Soot Emissions Using 3-D CFD Simulation*. In *SAE Technical Paper, No. 2005-01-2117* (2005).
74. Mei, Q., Liu, L. & Mansor, M. R. A. Investigation on spray combustion modeling for performance analysis of future low-and zero-carbon DI engine. *Energy* **1**, 131906 (2024).

## Acknowledgements

This study has been supported by the Recep Tayyip Erdogan University Development Foundation through the grant number 02025001002235.

The authors extend their appreciation to the Deanship of Scientific Research at King Khalid University, Saudi Arabia for funding this work through the Research Group Program under Grant No: RGP 2/127/45.

This work was supported by Tenaga Nasional Berhad (TNB) and UNITEN through the BOLD Refresh Postdoctoral Fellowships under Grant J510050002-IC-6 BOLDREFRESH2025-Centre of Excellence.

## Author contributions

Conceptualization—Harish Venu, Tiong Sieh Kiong; Investigation—Harish Venu and N.M. Razali; Methodology—Armin Rajabi, Hua-Rong Wei; Supervision, Validation—Tiong Sieh Kiong; Writing—original draft, Harish Venu and N.M. Razali; Review & editing—Armin Rajabi, Manzoore Elahi M. Soudagar, Erdem Cuce, V. Dhana Raju, and Naif Almakayee. Funding acquisition—T. M. Yunus Khan.

## Declarations

### Competing interests

The authors declare no competing interests.

### Additional information

**Correspondence** and requests for materials should be addressed to M.E.M.S. or E.C.

**Reprints and permissions information** is available at [www.nature.com/reprints](http://www.nature.com/reprints).

**Publisher's note** Springer Nature remains neutral with regard to jurisdictional claims in published maps and institutional affiliations.

**Open Access** This article is licensed under a Creative Commons Attribution-NonCommercial-NoDerivatives 4.0 International License, which permits any non-commercial use, sharing, distribution and reproduction in any medium or format, as long as you give appropriate credit to the original author(s) and the source, provide a link to the Creative Commons licence, and indicate if you modified the licensed material. You do not have permission under this licence to share adapted material derived from this article or parts of it. The images or other third party material in this article are included in the article's Creative Commons licence, unless indicated otherwise in a credit line to the material. If material is not included in the article's Creative Commons licence and your intended use is not permitted by statutory regulation or exceeds the permitted use, you will need to obtain permission directly from the copyright holder. To view a copy of this licence, visit <http://creativecommons.org/licenses/by-nc-nd/4.0/>.

© The Author(s) 2024